



Howcroft, C., Krauskopf, B., Lowenberg, M. H., & Neild, S. A. (2013). Influence of Variable Side-Stay Geometry on the Shimmy Dynamics of an Aircraft Dual-Wheel Main Landing Gear. *SIAM Journal on Applied Dynamical Systems*, 12(3), 1181-1209. 10.1137/120887643

Link to published version (if available):  
[10.1137/120887643](https://doi.org/10.1137/120887643)

[Link to publication record in Explore Bristol Research](#)  
PDF-document

## University of Bristol - Explore Bristol Research

### General rights

This document is made available in accordance with publisher policies. Please cite only the published version using the reference above. Full terms of use are available:  
<http://www.bristol.ac.uk/pure/about/ebr-terms.html>

### Take down policy

Explore Bristol Research is a digital archive and the intention is that deposited content should not be removed. However, if you believe that this version of the work breaches copyright law please contact [open-access@bristol.ac.uk](mailto:open-access@bristol.ac.uk) and include the following information in your message:

- Your contact details
- Bibliographic details for the item, including a URL
- An outline of the nature of the complaint

On receipt of your message the Open Access Team will immediately investigate your claim, make an initial judgement of the validity of the claim and, where appropriate, withdraw the item in question from public view.

## Influence of Variable Side-Stay Geometry on the Shimmy Dynamics of an Aircraft Dual-Wheel Main Landing Gear\*

Chris Howcroft<sup>†</sup>, Bernd Krauskopf<sup>‡</sup>, Mark H. Lowenberg<sup>§</sup>, and Simon A. Neild<sup>¶</sup>

**Abstract.** Commercial aircraft are designed to fly but also need to operate safely and efficiently as vehicles on the ground. During taxiing, take-off, and landing the landing gear must operate reliably over a wide range of forward velocities and vertical loads. Specifically, it must maintain straight rolling under a wide variety of operating conditions. It is well known, however, that under certain conditions the wheels of the landing gear may display unwanted oscillations, referred to as shimmy oscillations, during ground maneuvers. Such oscillations are highly unwanted from a safety and a ride-comfort perspective. In this paper we conduct a study into the occurrence of shimmy oscillations in a main landing gear (MLG) of a typical midsize passenger aircraft. Such a gear is characterized by a main strut attached to the wing spar with a side-stay that connects the main strut to an attachment point closer to the fuselage center line. Nonlinear equations of motion are developed for the specific case of a two-wheeled MLG configuration and allow for large angle deflections within the geometrical framework of the system. The dynamics of the MLG are expressed in terms of three degrees of freedom: torsional motion, in-plane motion, and out-of-plane motion (with respect to the side-stay plane). These are modeled by oscillators that are coupled directly through the geometric configuration of the system as well as through the tire/ground interface, which is modeled here by the von Schlippe stretched string approximation of the tire dynamics. The mathematical model is fully parameterized and parameters are chosen to represent a generic (rather than a specific) landing gear. In particular, the positions of the attachment points are fully parameterized so that any orientation of the side-stay plane can be considered. The occurrence of shimmy oscillations is studied by means of a two-parameter bifurcation analysis of the system in terms of the forward velocity of the aircraft and the vertical force acting on the gear. The effect of a changing side-stay plane orientation angle on the bifurcation diagram is investigated. We present a consistent picture that captures the transition of the two-parameter bifurcation diagram as a function of this angle, with a considerable complexity of regions of different types of shimmy oscillations for intermediate and realistic side-stay plane orientations. In particular, we find a region of tristability in which stable torsional, in-plane, and out-of-plane shimmy oscillations coexist.

**Key words.** aircraft ground dynamics, main landing gear model, shimmy oscillations, bifurcation analysis

**AMS subject classifications.** 70K30, 70K50, 34C15

**DOI.** 10.1137/120887643

---

\*Received by the editors August 9, 2012; accepted for publication (in revised form) by H. Dankowicz April 30, 2013; published electronically July 23, 2013.

<http://www.siam.org/journals/siads/12-3/88764.html>

<sup>†</sup>Department of Engineering Mathematics, University of Bristol, Bristol BS8 1TR, United Kingdom ([c.howcroft@bristol.ac.uk](mailto:c.howcroft@bristol.ac.uk)). The research of this author was supported by a Knowledge Transfer Network (KTN) Mathematics CASE Award from the Engineering and Physical Sciences Research Council (EPSRC) in collaboration with Airbus in the UK.

<sup>‡</sup>Department of Mathematics, The University of Auckland, Private Bag 92019, Auckland 1142, New Zealand ([b.krauskopf@auckland.ac.nz](mailto:b.krauskopf@auckland.ac.nz)).

<sup>§</sup>Department of Aerospace Engineering, University of Bristol, Bristol BS8 1TR, United Kingdom ([m.lowenberg@bristol.ac.uk](mailto:m.lowenberg@bristol.ac.uk)).

<sup>¶</sup>Department of Mechanical Engineering, University of Bristol, Bristol BS8 1TR, United Kingdom ([simon.neild@bristol.ac.uk](mailto:simon.neild@bristol.ac.uk)).

**1. Introduction.** The technical term *shimmy* is generally used to describe the self-sustained oscillations of a system with one or more rolling wheels and represents a relatively well-studied problem in engineering. Typical examples of shimmy with which the reader may be familiar range from the weaving of a towed trailer at high speeds to the sudden oscillation of a loose trolley wheel. The phenomenon first began to attract research interest in connection with the undesirable oscillation of the steering mechanism of early automobiles. These vehicles shared the common design elements of a single front axle rigidly connected to the front wheels, and the severity of the problem increased further with the development of balloon tires and front wheel brakes. The first major contribution toward an understanding of shimmy dynamics was provided in 1925 by Broulheit [6], who recognized the role of tire flexibility and side slip in the shimmy mechanism. Furthermore, he also argued that the energy required to drive shimmy oscillations was made available through the dynamics of the tires. This work is particularly significant as such considerations still form the basis of shimmy research today. Around the same time, Sensaud de Lavaud formulated a theory of shimmy involving a system with rigid tires and in 1927 published research showing shimmy oscillations in such a system [40, 41]. This emphasized the importance of structural flexibility in the shimmy mechanism—a conclusion supported in the work of Moreland [29]. In Sensaud de Lavaud’s later work [42] he goes on to highlight the possible advantages of independent front wheel suspensions. This modification later proved very effective, and the development of such suspension configurations in the early 1930s almost entirely eliminated the problem of automotive shimmy. However, around the same time the development of tricycle landing gear configurations on aircraft resulted in a substantial increase in incidence of nose landing gear (NLG) shimmy, consequently shifting research interest from automotive to aircraft applications. In fact, aircraft shimmy has largely dominated the literature ever since, and examples of such shimmy events in aircraft can be seen in [1, 17, 20, 28, 55]. For further information we direct the reader to the survey papers of Dengler, Goland, and Herrman [13] and Pritchard [34] as entry points to the literature.

Of particular significance to our research is the consideration of relevant system nonlinearities in the shimmy mechanism. The importance of these effects was realized by Temple in his 1941 paper [50] in which he considers the problem of large amplitude shimmy. There he points out that such oscillations may be excited by relatively small perturbations and that the resulting shimmy modes are highly nonlinear, meaning that their stability may not be predicted with linear methods. Similarly Rotta [39] states that linear analysis techniques can provide insight into the small amplitude stability of a system but that the determination of quantities such as shimmy amplitudes requires the consideration of system nonlinearities. Since these early works a multitude of modeling efforts have taken such nonlinearities into account. References [2, 3, 14, 26, 58] consider a range of effects, including Coulomb friction, torsional freeplay, spring hardening, nonlinear tire modeling, oleo damping, and impact dynamics.

One way of studying the effects of such nonlinearities on the dynamics of an aircraft landing gear system is to perform a bifurcation study of a suitable mathematical model by means of the numerical continuation of solutions and their bifurcations. The earliest application of these methods in an aerospace context came from Carroll and Mehra [7], who discussed the applicability of continuation methods to flight dynamics, identifying the main types of aircraft instability as described by bifurcations of the dynamic system. In [18], Goman, Zagainov, and Khrantsovsky discuss the applicability of a bifurcation and continuation methodology

to problems in flight dynamics (stall, spin, etc.), concluding that such methods are of great value for the analysis of aircraft dynamics both with and without flight control. Additional applications of such methods are also discussed in the journal special issue [51]. These methods continue to play an important role in the analysis of problems in aircraft flight dynamics, and recent examples of this approach include the study of rotorcraft aeroelastics [37] and of flight control systems via the continuation of control parameters [25]. Further examples are cited in the review paper of Paranjape, Sinha, and Ananthkrishnan [32] illustrating the use of bifurcation and continuation methods for aircraft trim and stability analysis.

Our focus in this work is on the dynamics of aircraft on the ground, and here examples of continuation analysis in the literature are more limited. In [10], Coetzee, Krauskopf, and Lowenberg discuss the usefulness of continuation methods in an industrial design context for the prediction of the low-speed ground turning of a civil aircraft and for medium-speed maneuvers [11]. Rankin et al. consider the stability of aircraft turning on the ground under constant thrust conditions [36] and find canard orbits in the loss of lateral turning stability [35]. In [9] Chen, Gu, and Liu use bifurcation methods to illustrate the dynamics of an NLG system both with and without active torsional damping control. Of particular interest for the study presented here is the work of Thota, Krauskopf, and Lowenberg [52, 53] on shimmy oscillations in an aircraft NLG. The papers present a bifurcation study of shimmy oscillations of an NLG with a single wheel in terms of the velocity of the aircraft and the downward force on the gear. This work was expanded in [54] to a dual-wheel configuration, which allowed for the assessment of the effects of gyroscopic forces and axle width on shimmy behavior of the NLG. Finally, we remark that although shimmy oscillations are a well-documented phenomenon in aircraft ground dynamics, as Shaw and Balachandran point out in the review paper [43], shimmy oscillations may appear in mechanical systems outside of an aerospace context—for example, in the dynamics of motorcycles [5, 27]. These mechanical systems have also attracted research interest, and examples of shimmy research employing numerical continuation techniques include the studies of an automobile under steady cornering conditions [12], the dynamics of a pulled wheel system [49], and the active steering control of a car [8].

In this paper we perform a bifurcation analysis of shimmy oscillations in a dual-wheel aircraft main landing gear (MLG). A key new aspect of this study—compared to an NLG as studied in [52, 53, 54]—is that the side-stay, which fixes the gear in the downlocked position, may be mounted in different orientations. For a typical NLG the side-stay plane (spanned by the side-stay and the main strut of the gear) does not have a lateral component (with respect to the direction of travel of the aircraft). The side-stay of an MLG on a typical civil aircraft, on the other hand, is mounted largely laterally, with its attachment point closer to the center of the fuselage; see Figure 1. Furthermore, the exact orientation of the side-stay plane differs from aircraft to aircraft, and as a result the geometric complexity of an MLG is generally greater than that of an NLG.

To study MLG oscillations we introduce a mathematical model that describes the motion of the system in terms of three degrees of freedom (DoFs): torsional rotation about the strut axis, in-plane motion in the side-stay plane, and out-of-plane motion perpendicular to the side-stay plane. These DoFs are modeled as damped oscillators, which are coupled geometrically via the MLG structure as well as via the forces that arise at the tire/ground interface. With an appropriate tire model of the contact dynamics of the dual wheel, we

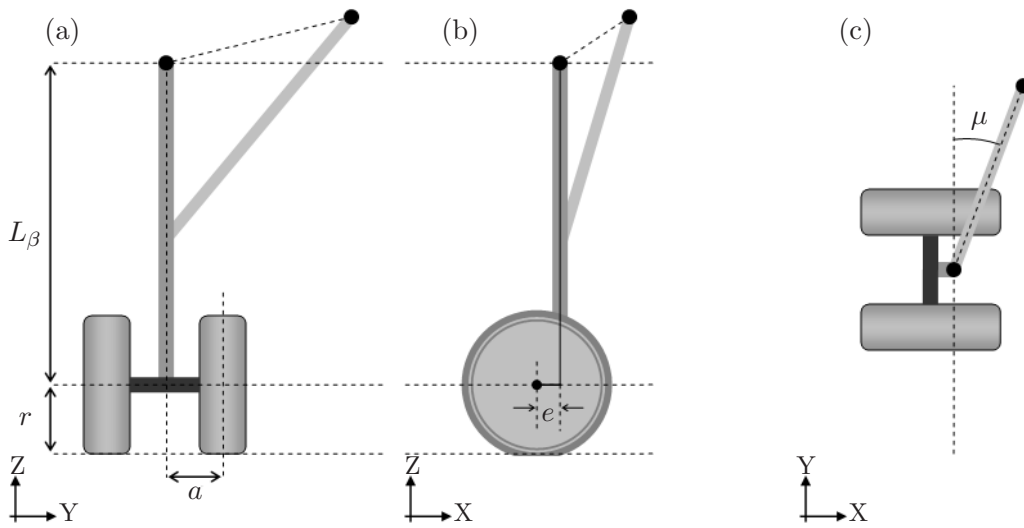


**Figure 1.** Parameterization of a typical dual-wheel MLG geometry. Global coordinates shown are aligned with  $X$  in the forward direction,  $Y$  to port and  $Z$  pointing vertically upward. For simplicity the gear is shown here for the zero-rake angle case, and, therefore, the main strut is aligned with the  $Z$ -axis.

obtain a seven-dimensional system of first-order ODEs for the dynamics of the MLG. The model is fully parameterized so that it can represent any given MLG geometry. In particular, we are able to study the sensitivity of the system to the orientation of the side-stay plane, which strongly influences the geometric coupling between the three DoFs. More specifically, for suitably chosen values of the side-stay orientation angle we present bifurcation diagrams in the parameter plane of aircraft velocity and vertical load on the MLG. Each such two-parameter bifurcation diagram is organized by curves of Hopf bifurcations, saddle-node bifurcations of periodic orbits, and torus bifurcations. They bound parameter regions in which one finds different types of shimmy oscillations of the system, which are characterized by the dominance of one or more of the three oscillatory DoFs. Considering the side-stay orientation angle  $\mu \in [0^\circ, 90^\circ]$  (where  $\mu = 0$  describes a laterally aligned side-stay and  $\mu = 90$  a side-stay aligned with the direction of travel; see Figure 1), we find a greatly increased complexity of (often coexisting) shimmy oscillations for intermediate (and realistic) values of  $\mu$ .

The paper is organized as follows. In section 2 we present the model of the MLG, which characterizes the motion of the system in terms of three oscillatory DoFs and the tire contact dynamics. In section 3 this model is used to determine the dynamics for the simplest geometric case of a side-stay that is perpendicular to the direction of travel and has an attachment point level with that of the main strut. The effect on the bifurcation diagram of changing the side-stay orientation angle is then studied in section 4. Finally, in section 5 we draw some conclusions and point to future work.

**2. Vector model of an MLG.** For our study we consider a typical MLG dual-wheel geometry, consisting of a main strut, side-stay, and axle assembly characterizing the MLG design of a wide array of aircraft. A representation of this geometry is shown in Figure 1.  $L_\beta$  denotes the length of the gear from the wheel axle center to the top of the main strut as

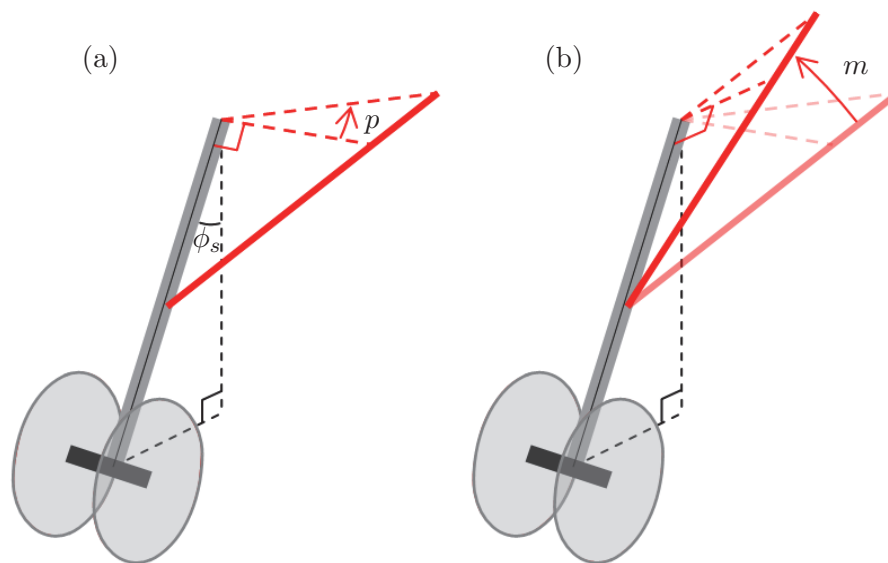


**Figure 2.** Angles  $m$  and  $p$  used to parameterize side-stay orientations, which are aligned relative to the main strut rather than the global coordinate system. For the case shown  $\phi_s \neq 0$  and  $e = 0$ .

indicated,  $r$  the radius of the tires,  $a$  their separation from the axle center, and  $e$  the caster length, expressing the shortest distance between the main strut and wheel axle center line. We allow the MLG to have a rake angle  $\phi_s$ , defined as the angle between the main strut and the vertical  $Z$ -axis. This angle is shown in Figure 2; for clarity we initially consider the zero-rake angle case in Figure 1.

An important feature of our model is that the orientation of the attachment points is fully parameterized by the angles  $\mu$  and  $\rho$ . This parameterization adds significant flexibility to our model, as in most cases the difference between aircraft MLG designs can be characterized simply as a change of this side-stay geometry. We use  $\rho$  to describe the inclination of these points (as shown in Figure 3) and  $\mu$  to describe the orientation of their projection in the  $(X, Y)$ -plane, taken from the  $Y$ -axis (shown in Figure 1). The MLG may even approach the configuration of an NLG as the parameter  $\mu$  approaches  $\pm 90^\circ$ , with the side-stay becoming the NLG drag-stay; compare with [52].

The presence of a side-stay in the system suggests a suitable treatment of the dynamics expressed in terms of three DoFs, two of which are defined with respect to the side-stay orientation. We refer to them as the torsional DoF  $\psi$ , the in-plane DoF  $\delta$  in the side-stay plane (spanned by the main strut and side-stay), and the out-of-plane DoF  $\beta$  in the direction perpendicular to the side-stay plane. In the formulation we consistently first apply  $\psi$ ,  $\delta$ , and then  $\beta$ . The three DoFs are shown in Figure 3 for the zero-rake angle case; for nonzero-rake angles the orientation of these DoFs is given by the vectors in Figure 5. Note that in Figure 3 we use the local coordinates  $(x, y, z)$  to define the orientation of  $\delta$  and  $\beta$ . Rotational vectors representing the orientation of these DoFs are also given in Figure 5.

By considering the dynamics of each of these DoFs (as well as an appropriate representation of the tire dynamics; see section 2.2) we will build a model of the MLG system. To



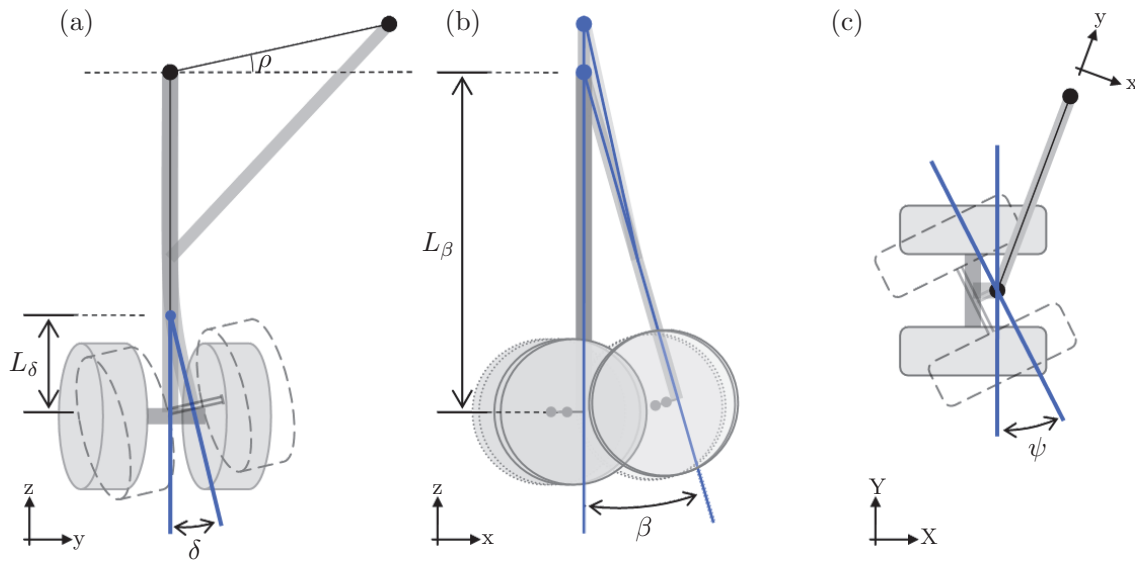


**Figure 3.** The dynamics of the MLG are expressed by the  $\delta$  DoF in the side-stay plane (a), the  $\beta$  DoF out of the side-stay plane (b), and the torsional  $\psi$  DoF (c). Due to the existence of the side-stay, in-plane bending of the main strut is approximated as an angular deflection about a point at distance  $L_\delta$  above the axle. Local coordinates  $(x, y, z)$  are defined with  $z$  aligned with the main strut,  $x$  perpendicular to the main strut and side-stay, and  $y$  chosen to complete the right-hand coordinate system. For the zero-rake angle case shown here  $z = Z$ .

facilitate the construction of this model we adopt a vector notation throughout. In particular, this allows us to resolve any forces affecting the gear into moments acting on the three DoFs, with the resultant terms expressed in a compact form without the necessity of providing simplifying assumptions. The vector formulation also casts the system in a more flexible framework, allowing for an easy incorporation of extra forces as well as changes to the geometry. This extra flexibility will prove particularly useful when we investigate the effects of changing the side-stay orientation angle in section 4.

**2.1. Equations of motion.** To begin with, we consider the free dynamics of the MLG system, that is, the behavior of the gear when freely suspended above the ground by its attachment points. Therefore, we first construct equations of motion expressing the dynamics of the system in terms of the generalized coordinate set  $\mathbf{q} = [\psi, \delta, \beta]$ . We note, however, that a number of assumptions are applied throughout this process in order to bring the equations in line with those used in [52] and [53], thus allowing validation of our model against existing results. Specifically, we do not include in the model a number of accelerative terms, namely, those due to

- centrifugal forces acting on the lateral DoF,

$$m_a L_\delta \sin(\delta - p) ((L_\beta - L_\delta) \cos p + L_\delta \cos(\delta - p)) \dot{\beta}^2,$$

- the conservation of longitudinal angular momentum,

$$2m_a L_\delta \sin(\delta - p) ((L_\beta - L_\delta) \cos p + L_\delta \cos(\delta - p)) \dot{\delta} \dot{\beta},$$

where  $m_a$  is the total mass of the wheel and axle assembly. The argument here is that the external forces acting on a landing gear in contact with the ground are very large, while terms representing effects such as these are much smaller; therefore, they do not contribute to the dynamics of the system in any significant way and can be disregarded. Another term not included in the system of equations is the gyroscopic force produced by the spinning wheel and axle components. This does in general have an effect on the dynamics of a landing gear system even given high external forces, as the angular rates of these components are high. Such gyroscopic effects act to further couple the DoFs considered [31, 33], and herein lies the motivation for their exclusion from this particular study, allowing us to determine the additional coupling arising from a variable side-stay orientation in isolation.

Such assumptions bring the model of the MLG system in line with that used in the work of Thota, Krauskopf, and Lowenberg [52, 53] and produce the following equations of motion, extended to allow for a side-stay of arbitrary orientation:

$$(2.1) \quad I_\psi \ddot{\psi} + c_\psi (\dot{\psi} + \dot{\beta} \sin p) + k_\psi (\psi + \beta \sin p) - M_\psi(\psi, \delta, \beta, \lambda) = 0,$$

$$(2.2) \quad I_\delta \ddot{\delta} + c_\delta \dot{\delta} + k_\delta \delta - M_\delta(\psi, \delta, \beta, \lambda) = 0,$$

$$(2.3) \quad I_\beta \ddot{\beta} \cos^2 p + \left[ (c_\beta + c_\psi \sin^2 p) \dot{\beta} + (c_\psi \sin p) \dot{\psi} \right] \\ + \left[ (k_\beta + k_\psi \sin^2 p) \beta + (k_\psi \sin p) \psi \right] - M_\beta(\psi, \delta, \beta, \lambda) = 0,$$

where the parameters  $I_{\psi,\delta,\beta}$ ,  $c_{\psi,\delta,\beta}$ , and  $k_{\psi,\delta,\beta}$  represent the inertial, damping, and stiffness values of their respective DoFs, and the terms  $M_{\psi,\delta,\beta}$  denote moment forces acting on the system, resolved into the three modal directions. Here  $\lambda$  is the lateral deflection of the tires, calculated from an appropriate tire model that is introduced next. The orientation of the MLG side-stay is expressed here via the introduction of the angles  $p$  and  $m$ , which give the relative positioning of the attachment points with respect to the  $(Y, z)$ -plane (shown in Figure 2), rather than the global coordinate system. We note that these angles coincide with  $\rho$  and  $\mu$  for the zero-rake angle case ( $\phi_s = 0$ ). From the angles  $p$  and  $m$  we can see that geometric independence of the  $\psi$  and  $\beta$  DoFs implies that  $p = 0$  (for  $p \neq 0$  any  $\beta$  motion of the system about the attachment points will also result in a twisting of the gear at the wheel axle).

**2.2. Tire model.** Having modeled the behavior of the free system (2.1)–(2.3), we now wish to capture the full dynamics of the MLG by considering the tire-ground interface and associated tire dynamics. These tire dynamics are necessary for the appearance of shimmy oscillation, extracting energy from the forward motion of the system and feeding it into the structural modes [57]. They also produce additional coupling between the DoFs of the system.

Hence, to fully model the MLG we must introduce an appropriate tire model. Since shimmy oscillations have been a recognized phenomenon for a long time it is perhaps unsurprising that a number of tire models have been developed and applied throughout the shimmy literature. The earliest of these models considered a tire meeting the ground at a single contact point [21], and such representations have since proved popular, particularly the model of Moreland [30]. Another modeling approach was introduced by von Schlippe and Dietrich, in 1941, who considered the concept of a stretched string with finite contact length to describe the mechanics of a rolling tire [56]. Since then a number of different tire models have been



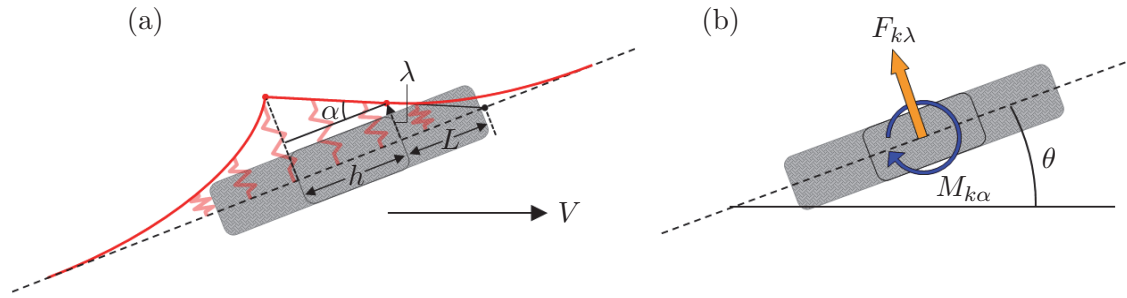


**Figure 4.** Panel (a) shows the von Schlippe straight line tangency assumption of the contact patch shape and resultant slip angle  $\alpha$  describing its orientation, and in panel (b) the angle  $\alpha$  is used to calculate tire forces  $F_{k\lambda}$  and  $M_{k\alpha}$  acting on the system.

suggested based on this stretched string concept, and these include the models of Kluiters [22], Rogers [38], and Pacejka [31]. In particular, Pacejka points out the importance of delay effects in the shimmy of an elastic tire, and recent efforts to incorporate this have prompted the use of delay differential equations (DDEs) in expressing delay and memory effects over the contact region [46, 47, 48].

For this study we employ the von Schlippe stretched string approximation of the tire dynamics based on [56]. This model is regarded in the literature as generally consistent with experimental data and unlike DDE representations is readily amenable to the numerical continuation tools used for this study. More information on these models can be found in the work of Koenig [23] and Besselink [4], who both provide comparisons between a number of stretched string variants; Smiley [44] also presents an overview and evaluation of a number of such models, showing that, in fact, many may be obtained via the approximation of a summarizing model based on the theory of von Schlippe and Dietrich. For our system the tire model takes the following form:

$$(2.4) \quad \dot{\lambda} + \frac{V}{L}\lambda + V u_{\lambda,X} + \frac{1}{2}(\mathbf{V}_{LCF} + \mathbf{V}_{RCF}) \cdot \mathbf{u}_{\lambda} = 0,$$

where  $\lambda$  is the lateral deformation of the tires,  $V$  is the forward velocity of the system (aligned with the  $X$ -direction), and  $L$  is the relaxation length of the tires; here  $u_{\lambda,X}$  denotes the  $X$  component of the lateral tire vector  $\mathbf{u}_{\lambda}$ ; see section 2.3. The terms  $\mathbf{V}_{LCF} \cdot \mathbf{u}_{\lambda}$  and  $\mathbf{V}_{RCF} \cdot \mathbf{u}_{\lambda}$  give the lateral velocity of the left and right wheels, respectively, where

$$\begin{aligned} \mathbf{V}_{LCF} &= \mathbf{u}_{\psi} \times (\mathbf{P}_{LCF} - \mathbf{P}_0) \dot{\psi} + \mathbf{u}_{\delta} \times (\mathbf{P}_{LCF} - \mathbf{P}_{\delta}) \dot{\delta} + \mathbf{u}_{\beta} \times (\mathbf{P}_{LCF} - \mathbf{P}_{\beta}) \dot{\beta}, \\ \mathbf{V}_{RCF} &= \mathbf{u}_{\psi} \times (\mathbf{P}_{RCF} - \mathbf{P}_0) \dot{\psi} + \mathbf{u}_{\delta} \times (\mathbf{P}_{RCF} - \mathbf{P}_{\delta}) \dot{\delta} + \mathbf{u}_{\beta} \times (\mathbf{P}_{RCF} - \mathbf{P}_{\beta}) \dot{\beta}. \end{aligned}$$

Again, these vectors are defined later in section 2.3.

With this tire model, we may use the lateral deflection  $\lambda$  to approximate the slip angle  $\alpha$  of the contact region, which we assume to have length  $h$ . This is based on the assumption that within this region the deflection of each tire, given by the red line in Figure 4, may be represented by a straight line continuing tangentially from the front of the contact patch. This allows the orientation of this region to be represented by the angle  $\alpha$ , which may be written

as

$$\alpha = \tan^{-1} \left( \frac{\lambda}{L} \right).$$

Knowledge of this angle allows us to model the reaction forces produced at the tires. They consist of a lateral reaction force  $F_{k\lambda}$  and a self-aligning moment  $M_{k\alpha}$ ; see Figure 4. References [45] and [52] provide expressions that may be used in approximating these terms; they are

$$(2.5) \quad F_{k\lambda} = k_\lambda \tan^{-1}(7.0 \tan \alpha) \cos(0.95 \tan^{-1}(7.0 \tan \alpha)) F_z,$$

$$(2.6) \quad M_{k\alpha} = \begin{cases} k_\alpha \alpha_m / \pi \sin(\pi \alpha / \alpha_m) F_z & \text{if } |\alpha| \leq \alpha_m, \\ 0 & \text{if } |\alpha| > \alpha_m, \end{cases}$$

where  $k_\lambda$  and  $k_\alpha$  are the lateral restoring and self-aligning coefficients of the tires, respectively,  $F_z$  is the vertical force acting on the system, and  $\alpha_m$  is the maximum slip angle beyond which we take  $M_{k\alpha} = 0$ .

**2.3. Derivation of force terms.** We must now determine expressions for the moments acting in each of the three modal directions, given by the terms  $M_{\psi, \delta, \beta}$  in (2.1)–(2.3). These forces and moments acting on the system are a consequence of the weight of the aircraft and the MLG, the forces produced at the tire-ground interface, and the rolling stiffness of the dual-wheel configuration. To model their effects on the system we must resolve the moments they create in each of the modal directions. In general, these moments take the form  $\mathbf{P} \times \mathbf{F} \cdot \mathbf{u}$ , where  $\mathbf{F}$  is the applied force,  $\mathbf{P}$  is the vector of the appropriate moment arm, and  $\mathbf{u}$  is the unit vector expressing the orientation of the DoF in question. We therefore define a series of position vectors for the MLG representing important geometric points as well as the points of force application; they are displayed graphically in Figure 5 and are given as

$$\begin{aligned} \mathbf{P}_\delta &= (0, 0, 0), & \mathbf{P}_{LC} &= \mathbf{P}_L + r \mathbf{u}_r, \\ \mathbf{P}_\beta &= R(\mathbf{u}_\beta, \beta) R(-\mathbf{e}_Y, \phi_0) (0, 0, L_\beta - L_\delta), & \mathbf{P}_{RC} &= \mathbf{P}_R + r \mathbf{u}_r, \\ \mathbf{P}_0 &= R(\mathbf{u}_\beta, \beta) R(\mathbf{u}_{\delta 0}, \delta) R(-\mathbf{e}_Y, \phi_0) (0, 0, -L_\delta), & \mathbf{P}_{LCF} &= \mathbf{P}_{LC} + 1/2 h \mathbf{u}_f, \\ \mathbf{P}_L &= R(\mathbf{u}_\beta, \beta) R(\mathbf{u}_{\delta 0}, \delta) R(\mathbf{u}_{\psi 0}, \psi_s) R(-\mathbf{e}_Y, \phi_0) (-e, a, -L_\delta), & \mathbf{P}_{RCF} &= \mathbf{P}_{RC} + 1/2 h \mathbf{u}_f, \\ \mathbf{P}_R &= R(\mathbf{u}_\beta, \beta) R(\mathbf{u}_{\delta 0}, \delta) R(\mathbf{u}_{\psi 0}, \psi_s) R(-\mathbf{e}_Y, \phi_0) (-e, -a, -L_\delta), \end{aligned}$$

where  $R(\mathbf{v}, \theta)$  denotes the rotation matrix corresponding to a rotation of  $\theta$  radians about the vector  $\mathbf{v}$ . Moreover,  $\mathbf{e}_X$ ,  $\mathbf{e}_Y$ ,  $\mathbf{e}_Z$  are unit vectors in the  $X$ ,  $Y$ , and  $Z$  global directions, respectively,  $\phi_s$  is the (dynamically changing) rake angle of the MLG, and  $\phi_0$  is its static value for  $(\psi, \delta, \beta) = \mathbf{0}$ .

We also define the following vectors describing the orientation of the MLG DoFs, as well as the orientation of various constituent parts of the system; these are shown in Figure 5 and

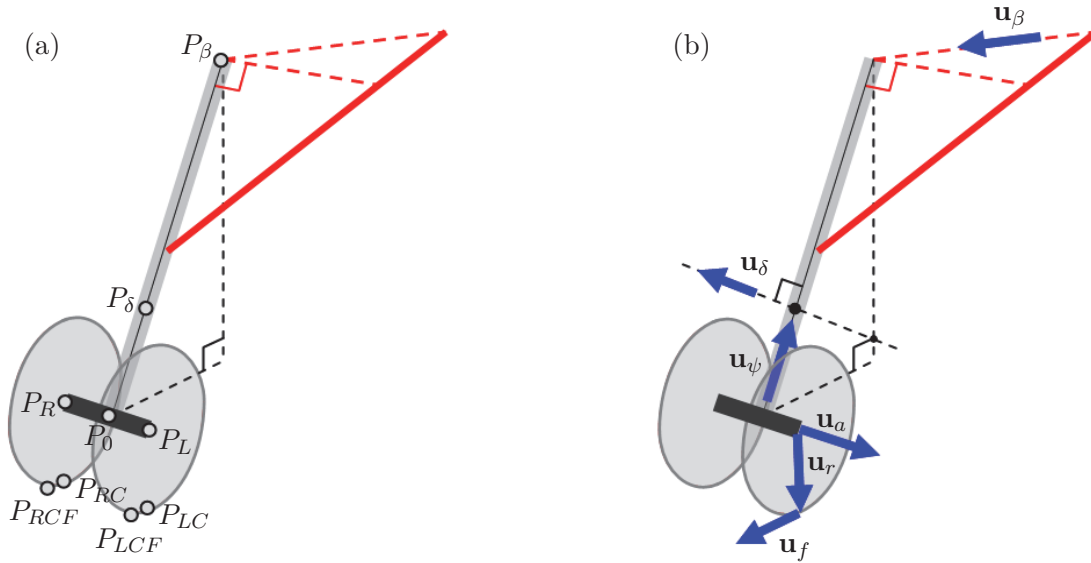


**Figure 5.** Points (a) and unit vectors (b) allowing calculation of the moments acting on the system. The point  $P_0$  lies along the center line of the main strut, offset from the wheel axle  $\overrightarrow{P_R P_L}$  by the caster length  $e$ .

are written in the global reference frame as

$$\mathbf{u}_{\psi 0} = \begin{pmatrix} -\sin \phi_0 \\ 0 \\ \cos \phi_0 \end{pmatrix}, \quad \mathbf{u}_\beta = \begin{pmatrix} -\cos \rho \sin \mu \\ -\cos \rho \cos \mu \\ -\sin \rho \end{pmatrix}, \quad \mathbf{u}_{\delta 0} = \begin{pmatrix} \cos m \cos \phi_0 \\ -\sin m \\ \cos m \sin \phi_0 \end{pmatrix},$$

$$\mathbf{u}_\psi = R(\mathbf{u}_\beta, \beta)R(\mathbf{u}_{\delta 0}, \delta)\mathbf{u}_{\psi 0},$$

$$\mathbf{u}_\delta = R(\mathbf{u}_\beta, \beta)\mathbf{u}_{\delta 0},$$

$$\mathbf{u}_\lambda = \frac{1}{|(\mathbf{u}_{a,X}, \mathbf{u}_{a,Y}, 0)|}(\mathbf{u}_{a,X}, \mathbf{u}_{a,Y}, 0),$$

$$\mathbf{u}_a = R(\mathbf{u}_\beta, \beta)R(\mathbf{u}_{\delta 0}, \delta)R(\mathbf{u}_{\psi 0}, \psi_s)\mathbf{e}_Y,$$

$$\mathbf{u}_f = \frac{1}{|(\mathbf{u}_{a,Y}, -\mathbf{u}_{a,X}, 0)|}(\mathbf{u}_{a,Y}, -\mathbf{u}_{a,X}, 0),$$

$$\mathbf{u}_r = R(\mathbf{u}_f, -\pi/2)\mathbf{u}_a.$$

Given these vectors, we are now able to define the moment terms acting on the MLG system, which may be written as

$$(2.7) \quad M_\psi = [(\mathbf{P}_{LC} - \mathbf{P}_0) \times \mathbf{F}_L + (\mathbf{P}_{RC} - \mathbf{P}_0) \times \mathbf{F}_R + (\mathbf{P}_C - \mathbf{P}_0) \times \mathbf{F}_\lambda - \mathbf{M}_\alpha] \cdot \mathbf{u}_\psi,$$

$$(2.8) \quad M_\delta = [(\mathbf{P}_{LC} - \mathbf{P}_\delta) \times \mathbf{F}_L + (\mathbf{P}_{RC} - \mathbf{P}_\delta) \times \mathbf{F}_R + (\mathbf{P}_C - \mathbf{P}_\delta) \times \mathbf{F}_\lambda] \cdot \mathbf{u}_\delta,$$

$$M_\beta^* = [(\mathbf{P}_{LC} - \mathbf{P}_\beta) \times \mathbf{F}_L + (\mathbf{P}_{RC} - \mathbf{P}_\beta) \times \mathbf{F}_R + (\mathbf{P}_C - \mathbf{P}_\beta) \times \mathbf{F}_\lambda] \cdot \mathbf{u}_\beta,$$

$$(2.9) \quad M_\beta = M_\beta^* - M_\psi(\mathbf{u}_\beta \cdot \mathbf{u}_\psi),$$

$$\mathbf{P}_C = \frac{1}{2}(\mathbf{P}_{LC} + \mathbf{P}_{RC}).$$

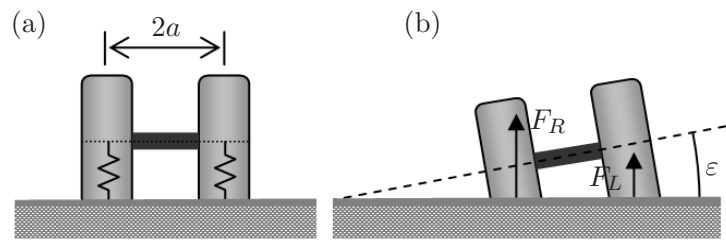


**Figure 6.** Dual-wheel configuration with separation distance  $2a$  (a). Left ( $F_L$ ) and right ( $F_R$ ) reaction forces acting on the system (b) are calculated using a static force balance for an axle inclined at an angle  $\varepsilon$  to the ground plane.

Here  $M_\beta$  takes a more complex form due to the coupling between  $\psi$  and  $\beta$ . The term  $\mathbf{F}_\lambda = \mathbf{u}_\lambda F_{k\lambda}$  represents the combined side force produced by both tires.

We split the vertical force  $F_z$  acting on the system into separate reaction forces  $\mathbf{F}_L$  and  $\mathbf{F}_R$ . This is achieved by considering a static force balance on the wheel assembly for tires of vertical stiffness  $k_t$  and an angle  $\varepsilon$  between the wheel axle and ground plane; see Figure 6. This allows these reaction forces to be written as

$$\mathbf{F}_{L,R} = (1/2F_z \mp a\varepsilon k_t) \mathbf{e}_z,$$

where  $\varepsilon = \sin^{-1}(u_{a,z})$ .

Finally, we consider the term  $\mathbf{M}_\alpha$  in (2.7), which represents the restoring moment exerted by the tires onto the landing gear. It is given by

$$\mathbf{M}_\alpha = \left( M_{k\alpha} + c_\lambda \dot{\psi} u_{\psi,z} V^{-1} \right) \mathbf{e}_z$$

and is a consequence of both the stiffness and damping properties associated with the warping of the tire contact patch regions. Here  $c_\lambda$  denotes the rotational damping of the contact patch area, having a decreasing effect on the system dynamics as the forward velocity of the system increases, and  $M_{k\alpha}$  represents the rotational stiffness and is given by (2.6). We assume that the effect of this restoring force is felt only by the torsional DoF of the system, and so the term appears only in (2.7).

With the addition of these terms we may now represent the full dynamics of the MLG as given by (2.1)–(2.4) with the moment terms as defined in (2.7)–(2.9). To study the behavior of these equations, we also require a representative set of parameter values for an MLG. We choose the values as listed in Table 1, which are taken in part from [52] with a careful selection of the other parameters to ensure realistic and sufficiently distinct linear frequencies of 9.81 Hz, 16.05 Hz, and 13.63 Hz for the  $\psi$ ,  $\delta$ , and  $\beta$  DoFs, respectively. Although these parameter values do not come from a specific civil aircraft MLG, they serve to represent a generic landing gear system that may experience shimmy instability. In particular, they allow us to study the additional effects of a variable side-stay geometry on the shimmy dynamics. Note that the ranges of the continuation parameters  $V$  and  $F_z$  are deliberately chosen larger than their operational ranges in order to ensure that all features of the bifurcation diagrams are captured.

Table 1

Parameters and their values as used in the analysis of the MLG.

| Symbol                         | MLG parameter                                 | Value             | Units                              |
|--------------------------------|---|-------------------|------------------------------------|
| <i>Geometric parameters</i>    |   |                   |                                    |
| $\rho$                         | attachment point inclination                  | 0                 | deg                                |
| $\mu$                          | horizontal attachment point orientation angle | 0 – 90            | deg                                |
| $e$                            | caster length                                 | 0.12              | m                                  |
| $\phi_0$                       | static rake angle                             | 0.05236           | rad ( $3^\circ$ )                  |
| $a$                            | half track width                              | 0.25              | m                                  |
| $L_\delta$                     | radius of in-plane deflection                 | 0.75              | m                                  |
| $L_\beta$                      | gear length                                   | 2.5               | m                                  |
| <i>Structural parameters</i>   |   |                   |                                    |
| $I_\psi$                       | torsional inertia                             | 100               | kg m <sup>2</sup>                  |
| $I_\delta$                     | in-plane inertia                              | 600               | kg m <sup>2</sup>                  |
| $I_\beta$                      | out-of-plane inertia                          | 750               | kg m <sup>2</sup>                  |
| $c_\psi$                       | torsional damping                             | 300               | N m s rad <sup>-1</sup>            |
| $c_\delta$                     | in-plane damping                              | 300               | N m s rad <sup>-1</sup>            |
| $c_\beta$                      | out-of-plane damping                          | 300               | N m s rad <sup>-1</sup>            |
| $k_\psi$                       | torsional stiffness                           | $3.8 \times 10^5$ | N m rad <sup>-1</sup>              |
| $k_\delta$                     | in-plane stiffness                            | $6.1 \times 10^6$ | N m rad <sup>-1</sup>              |
| $k_\beta$                      | out-of-plane stiffness                        | $5.5 \times 10^6$ | N m rad <sup>-1</sup>              |
| <i>Tire parameters</i>         |   |                   |                                    |
| $r$                            | tire radius                                   | 0.362             | m                                  |
| $h$                            | contact patch length                          | 0.1               | m                                  |
| $L$                            | relaxation length                             | 0.3               | m                                  |
| $k_t$                          | vertical tire stiffness                       | $7 \times 10^5$   | N m <sup>-1</sup>                  |
| $k_\alpha$                     | tire self-aligning coefficient                | 1.0               | m                                  |
| $k_\lambda$                    | tire lateral restoring coefficient            | 0.002             | rad <sup>-1</sup>                  |
| $c_\lambda$                    | tire damping coefficient                      | 570               | N m <sup>2</sup> rad <sup>-1</sup> |
| $\alpha_m$                     | maximum slip angle                            | 0.1745            | rad ( $10^\circ$ )                 |
| <i>Continuation parameters</i> |   |                   |                                    |
| $V$                            | forward velocity                              | 0 – 350           | m s <sup>-1</sup>                  |
| $F_z$                          | vertical force                                | 0 – $10^6$        | N                                  |

**3. Analysis of the perpendicular case  $\mu = 0$ .** We now turn our attention to the simplest side-stay orientation of the MLG, in which the line between the attachment points is horizontal and perpendicular to the direction of travel. We therefore set  $\rho = 0$  throughout and consider first the case that  $\mu = 0$ ; in turn this implies that both  $p = 0$  and  $m = 0$ ; see Figure 2. Consequently, in this case geometric coupling is small and the DoFs couple through the tire forces. Moreover, the in-plane DoF  $\delta$  corresponds to motion lateral to the direction of travel of the aircraft, while the out-of-plane DoF  $\beta$  corresponds to motion in the longitudinal direction of the aircraft. Hence, based on the observations in [52, 53] for an NLG, one would expect  $\delta$  to play a big role in the dynamics, with negligible coupling to  $\beta$  for this special case of  $\mu = 0$ . In the following sections we provide examples of the different types of shimmy oscillations of the MLG and then use a bifurcation analysis to determine the parameter regions in the  $(V, F_z)$ -plane of forward velocity and vertical force, in which this behavior may be observed.

**3.1. Examples of shimmy oscillations.** To illustrate the existence of shimmy oscillations we numerically integrate (2.1)–(2.4) over time. Figures 7 and 8 give resulting time series

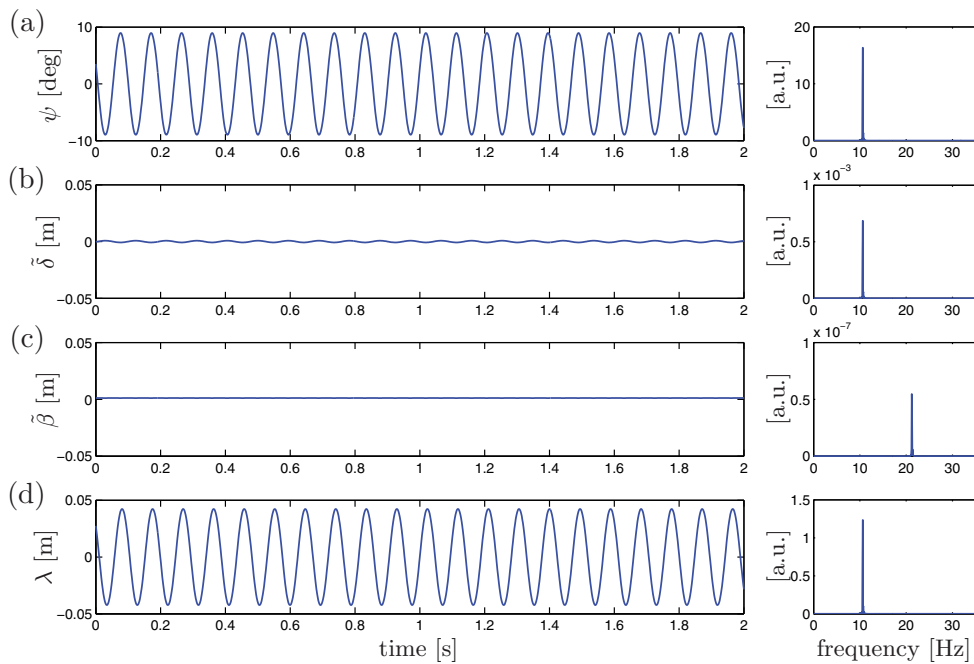


**Figure 7.** Torsional  $\psi$ -shimmy oscillations of the MLG with  $\mu = 0$  for  $V = 40$  m/s and  $F_z = 2 \times 10^5$  N. Shown are time series and the corresponding frequency spectra (in arbitrary units) of the torsional angle  $\psi$ , of the deflections  $\tilde{\delta}$  and  $\tilde{\beta}$ , and of the tire deflection  $\lambda$ .

for  $\psi$ ,  $\tilde{\delta}$ ,  $\tilde{\beta}$ , and  $\lambda$ , shown along with the corresponding frequency spectra. Throughout, the magnitude of the torsional DoF  $\psi$  is given in degrees, while the  $\delta$  and  $\beta$  DoFs are represented by the resulting deflections  $\tilde{\delta}$  and  $\tilde{\beta}$  at the bottom of the strut (at the point  $\triangle \mathbf{P}_0$  in Figure 5(a)); note that this definition is slightly different from that used in [52, 53], where the deflections are considered at ground level.

Figure 7 is for  $V = 40$  m/s and  $F_z = 2 \times 10^5$  N. We see that for this case all three DoFs display oscillatory motion but that torsional motion  $\psi$  dominates the response with a relatively large amplitude of nearly  $10^\circ$  degrees. In comparison, the  $\delta$  and  $\beta$  DoFs produce deflections  $\tilde{\delta}$  and  $\tilde{\beta}$  at the strut tip in the submillimeter range. Furthermore, we note that both  $\psi$  and  $\delta$  are locked into a frequency of  $\sim 10.6$  Hz with  $\beta$  oscillating at a frequency of twice this value. This characteristic frequency lies closest to the linear torsional frequency of 9.8 Hz, further emphasizing the torsional dominance within this response. As a final clarification we note that the lateral deflection  $\lambda$  of the tires shows periodic dynamics at the frequency and phase of the torsional DoF. Therefore, based on these results we determine that for this choice of parameters the MLG displays torsional or  $\psi$ -shimmy with the system passively following  $\psi$  in-phase.

Figure 8 shows the MLG response for  $V = 100$  m/s and  $F_z = 4 \times 10^5$  N. Again we observe oscillatory behavior of the system; however, the in-plane DoF  $\delta$  is now dominating the response. Moreover, this happens at a frequency of about 15.5 Hz, which now lies closest to the linear frequency of  $\delta$  of 16.1 Hz. We also note that the lateral tire deflection  $\lambda$  now



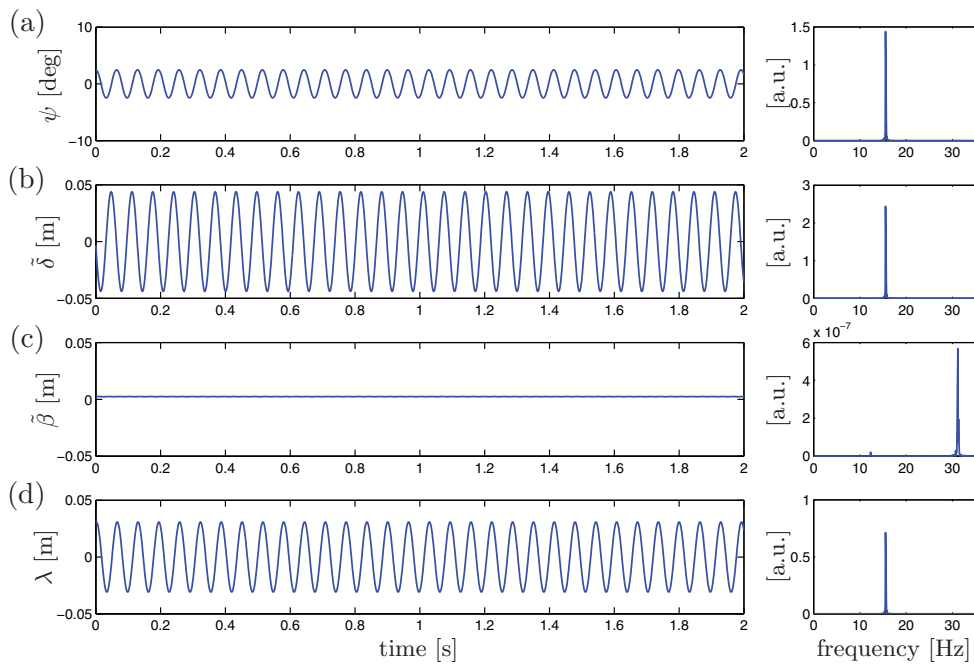


**Figure 8.** Lateral  $\delta$ -shimmy oscillations of the MLG with  $\mu = 0$  for  $V = 100$  m/s and  $F_z = 4 \times 10^5$  N. Shown are time series and the corresponding frequency spectra (in arbitrary units) of the torsional angle  $\psi$ , of the deflections  $\tilde{\delta}$  and  $\tilde{\beta}$ , and of the tire deflection  $\lambda$ .

oscillates with the frequency of the  $\delta$  DoF with a phase shift of  $\pi/2$  rad. As before, this observation may be used to identify this type of shimmy as in-plane or  $\delta$ -shimmy. Since the side-stay orientation angle  $\mu$  is zero, the  $\delta$  DoF in the side-stay plane is perpendicular to the direction of travel of the aircraft. Therefore,  $\delta$ -shimmy is also referred to as lateral shimmy of the MLG in this case, which is still justified when  $\mu$  is sufficiently small.

Overall, we observe that, depending on the parameter range in question, the system may display different types of shimmy oscillations, each corresponding to a different characteristic frequency, with the MLG experiencing different contributions from each of the three DoFs. Another point to note is that we have not yet seen out-of-plane or  $\beta$ -shimmy oscillations, where the  $\beta$  DoF is dominant in the MLG response. In the two cases of shimmy oscillations presented, the magnitude of  $\beta$  remains very small, while it passively follows the  $\psi$  or  $\delta$  DoF through coupling via the tire. Any larger perturbations to the  $\beta$  DoF simply cause it to perform damped oscillations at its own frequency, thus returning to a small and passive amplitude response. For an MLG with a perpendicular side-stay with  $\mu = 0$  the  $\beta$  DoF lies in the direction of travel of the aircraft. Oscillations in  $\beta$  are, hence, also referred to as longitudinal shimmy of the MLG when  $\mu$  is sufficiently small. In other words, we did not find longitudinal shimmy oscillations when  $\mu = 0$ , which can be attributed to the fact that the  $\beta$  DoF is not sufficiently coupled with the other DoFs to contribute to the shimmy dynamics. This finding agrees with the results in [52] for an NLG model represented by longitudinal, lateral, and torsional DoFs. Therefore, in this section that considers the case  $\mu = 0$ , we

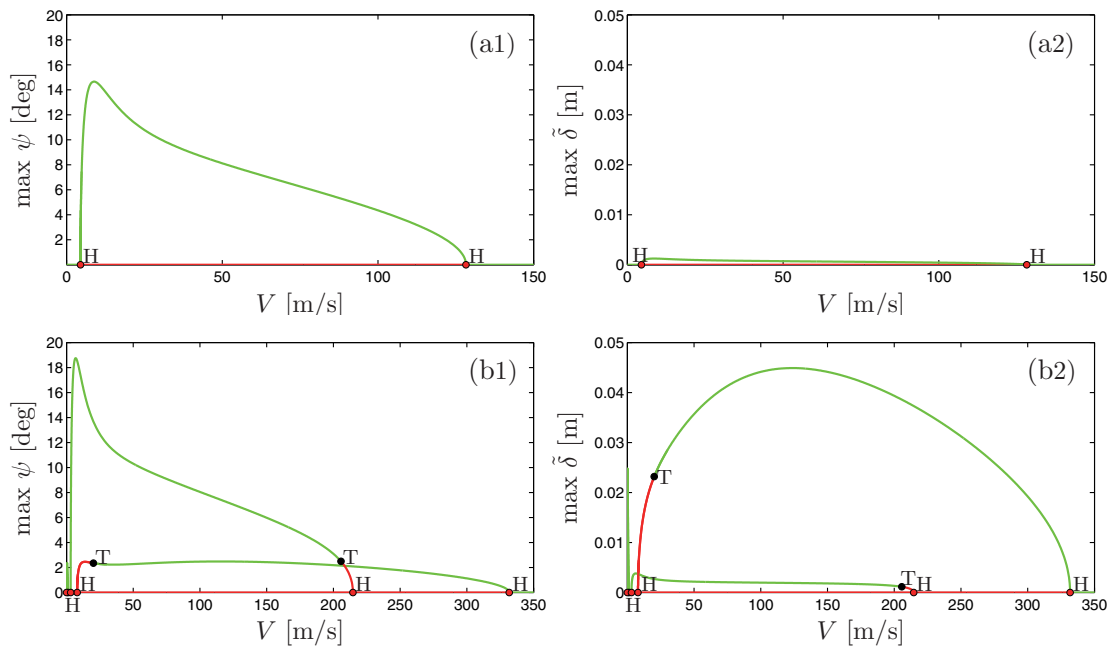


**Figure 9.** One-parameter bifurcation diagrams in  $V$  of the MLG with  $\mu = 0$  for a vertical force of  $F_z = 2 \times 10^5$  N in panels (a) and of  $F_z = 4 \times 10^5$  N in panels (b); shown are the maxima of the torsional angle  $\psi$  (left column) and of the in-plane deflection  $\tilde{\delta}$  (right column). Stable solutions are green, and unstable solutions are red; Hopf bifurcation points (H) are shown as red dots, and torus bifurcation points (T) as black dots.

restrict ourselves to showing only torsional  $\psi$  and (lateral) in-plane  $\delta$  motion.

**3.2. One-parameter continuation.** We now identify the parameter regions in which the MLG system may experience shimmy oscillations. We choose as our bifurcation parameter the forward velocity of the system  $V$ , while fixing  $F_z$  at a specific value and setting the other parameters as given in Table 1. This is a natural choice of bifurcation parameter as, in reality, the shimmy oscillations of landing gear systems are often observed only within a specific velocity range, suggesting an inherent sensitivity to variations in its value. One-parameter bifurcation diagrams are obtained with the continuation software AUTO [15]; to reflect our previous examples we choose values for the loading force  $F_z$  that match those already considered. Figures 9(a1) and (a2) show results for  $F_z = 2 \times 10^5$  N, indicating oscillatory solutions in terms of the amplitudes of the torsional DoF  $\psi$  and of the deflection  $\tilde{\delta}$  of the in-plane  $\delta$  DoF, respectively. Nonoscillatory straight-line rolling of the MLG is given by the zero-amplitude solution, which exists over the entire velocity range considered. However, as the forward velocity is increased, the stability of this straight-rolling solution changes: stability is lost and then regained when two supercritical Hopf bifurcation points are passed. These two bifurcation points are connected by a branch of stable periodic orbits, indicating the appearance of shimmy oscillations in the dynamics. Within the velocity range bounded by the two Hopf points the dynamics of the MLG will move away from the straight-rolling solution, and one observes the onset of shimmy oscillations, with amplitudes of  $\psi$  and  $\tilde{\delta}$  as shown in the figure (the amplitude of  $\tilde{\beta}$  remains extremely small throughout and is not

shown). We note from Figure 9(a) that the (torsional)  $\psi$ -component of this periodic solution is significantly greater than the (lateral)  $\tilde{\delta}$ -component, and indeed the entire branch of periodic orbits represents torsional  $\psi$ -shimmy; compare with Figure 7.

Figures 9(b1) and (b2) show one-parameter bifurcation diagrams for a loading force of  $F_z = 4 \times 10^5$  N. Apart from the previous branch of periodic orbits representing torsional shimmy, we now note the existence of a second branch of periodic solutions connecting a second pair of Hopf bifurcation points. The amplitudes of  $\psi$  and  $\tilde{\delta}$  along this branch show that the oscillations have a strong  $\delta$ -component, and we conclude that this branch represents (lateral) in-plane  $\delta$ -shimmy of the MLG; see Figure 8. Regarding the stability of the system, from Figures 9(b1) and (b2) we note that the straight-rolling solution is again unstable over the entire velocity range spanned by the periodic orbits. For lower values of the forward velocity we see that this results in torsional shimmy oscillations, whereas for higher velocity values the MLG experiences lateral shimmy. We also note that there exists a velocity range (here  $V \in (19.5, 205.7)$ ), bounded by torus bifurcation points, over which both periodic solutions are stable. Depending on the initial condition of the system and the presence of external perturbations, one may see either torsional or lateral shimmy in the MLG response for  $\mu = 0$ .

**3.3. Two-parameter bifurcation diagram.** Motivated by the results of the previous section, we now explore the system dynamics for a continuous range of the vertical force  $F_z$  rather than for the two discrete values previously considered. We therefore continue the codimension-one bifurcations identified in the previous section in the two-parameter  $(V, F_z)$ -plane of forward velocity  $V$  and loading force  $F_z$ . Figure 10 shows the resulting bifurcation diagram. It consists of a closed curve of Hopf bifurcations that intersects a second Hopf bifurcation curve at a pair of Hopf–Hopf points (HH). These codimension-two points are important in determining the local structure of the dynamics, and, as expected from general bifurcation theory, they lead to the emergence of two curves of torus (or Neimark–Sacker) bifurcations, the lower of which forms part of the stability boundary where in-plane  $\delta$  oscillations become stable. We also see curves of saddle-node (or fold) bifurcations of periodic orbits—emanating from degenerate Hopf points (DH) of the closed Hopf bifurcation curve—that act as further stability boundaries of the system. In particular, they form the boundaries of torsional shimmy oscillations for higher values of  $F_z$  and are, in fact, parts of a single fold curve connecting the two degenerate Hopf points.

Overall, the bifurcation diagram in the  $(V, F_z)$ -plane provides a global view of the dynamics of the MLG. The nonshaded region at the bottom of Figure 10 shows the desirable parameter region in which the nonoscillatory straight-rolling solution is stable. As the loading force is increased, this solution loses stability; this results in shimmy oscillations, which may be torsional or in-plane (lateral) in nature (depicted by left- and right-slanted shading, respectively). In agreement with what we saw in the last section, only torsional shimmy may be observed for low values of  $F_z$ . Lateral shimmy, on the other hand, may be found for larger loading forces, and it may coexist with torsional shimmy in a large region of bistability. A final point to note is that the bifurcation diagram in Figure 10 also serves to validate our model against existing results. Specifically, we see that our MLG model for  $\mu = 0$  has the same qualitative features as were found in [52] for a study of an NLG (with similar parameters and modeling assumptions). Indeed, for  $\mu = 0$  our model reproduces many of the dynamical

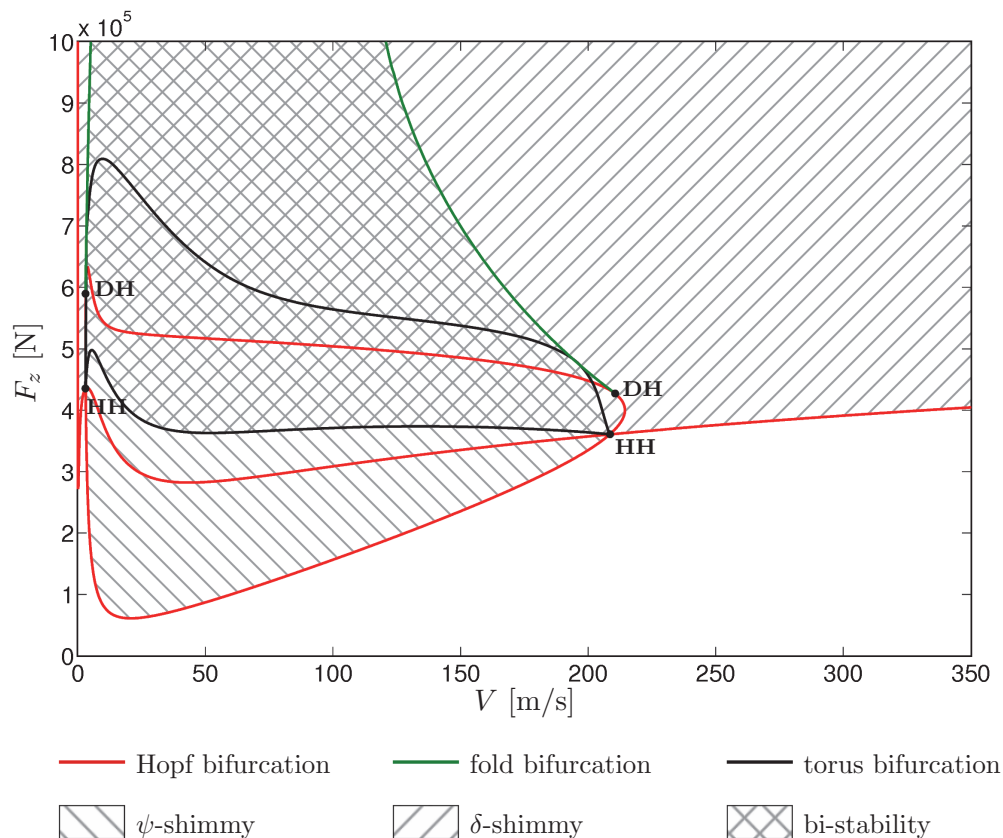


**Figure 10.** Bifurcation diagram in the  $(V, F_z)$ -plane of the MLG for  $\mu = 0$  with regions of torsional  $\psi$ -shimmy and with (lateral) in-plane  $\delta$ -shimmy oscillations. The points labeled HH and DH are codimension-two double Hopf and degenerate Hopf points, respectively.

characteristics found in NLG shimmy, including the presence of bistability.

**4. Effect of side-stay orientation angle  $\mu$ .** The bifurcation diagram in the  $(V, F_z)$ -plane in Figure 10 and the associated regions of different types of shimmy oscillations depend on the values of other parameters. We focus now on the effect of changing the side-stay angle  $\mu$  over the range  $\mu \in [0^\circ, 90^\circ]$ . This parameter is of specific interest, because  $\mu$  varies greatly from aircraft to aircraft and, in general, cannot be assumed to be zero or even small. Note that for nonzero values of  $\mu$  the orientation of the out-of-plane DoF  $\beta$  differs from the orientation of the tires. Via the tire dynamics this leads in turn to an increasing geometric coupling between all three DoFs (which is not present for the special case  $\mu = 0$ ). Moreover, for  $\mu \neq 0$  the  $\delta$  and  $\beta$  DoFs are no longer perfectly aligned with the lateral and longitudinal directions with respect to the direction of travel. Rather,  $\delta$  and  $\beta$  both represent lateral as well as longitudinal components for intermediate values of  $\mu$  until for  $\mu = 90^\circ$  their roles are exchanged, with  $\delta$  being a purely longitudinal motion and  $\beta$  being a purely lateral motion with respect to the direction of travel. In order to study the effect of this geometric coupling between the three DoFs  $\psi$ ,  $\delta$ , and  $\beta$ , we consider how the bifurcation diagram in the  $(V, F_z)$ -plane changes with

the side-stay angle  $\mu$ ; all other parameters remain fixed as specified in Table 1.

**4.1. Hopf frequency diagrams.** The curves of Hopf bifurcations play an important role in the dynamics of the MLG system: they generate different types of shimmy oscillations and are largely responsible for the overall structure of the bifurcation diagram in the  $(V, F_z)$ -plane. For this reason we first consider how the Hopf bifurcation curves alone change when the side-stay angle  $\mu$  is increased from  $\mu = 0$ . Since types of shimmy oscillations are characterized by having a frequency close to the linear frequency of the corresponding DoF, it is of interest to also consider the frequencies of the periodic orbits that bifurcate from the Hopf bifurcations. We therefore construct two-parameter diagrams in the  $(V, F_z)$ -plane of Hopf bifurcation curves, where color represents the frequency of the bifurcating periodic solutions as determined from the purely imaginary eigenvalues.

Figure 11 shows this type of Hopf frequency diagram for several representative values of  $\mu$  ranging from  $0^\circ$  to  $90^\circ$ . The corresponding color map shows the linear frequencies of the  $\psi$ ,  $\delta$ , and  $\beta$  DoFs as blue, red, and light green, respectively. Overall, one notices considerable changes in the Hopf bifurcation curves when  $\mu$  is increased from  $\mu = 0$  to  $\mu = 90^\circ$ . These two extreme values of  $\mu$  represent the simplest cases of the MLG system with effectively only two contributions to shimmy oscillation frequencies present in the dynamics: that of the  $\psi$  and  $\delta$  DoFs for  $\mu = 0$ , and that of the  $\psi$  and  $\beta$  DoFs for  $\mu = 90^\circ$ . Recall that  $\delta$  is defined as motion in the plane of the side-stay, while  $\beta$  models motion perpendicular to the side-stay plane. Hence,  $\beta$  is aligned with the direction of aircraft motion only for small values of the side-stay angle  $\mu$ . For  $\mu$  near  $90^\circ$ , on the other hand, the  $\delta$  DoF is aligned with the aircraft longitudinal direction; hence, it is geometrically uncoupled from the other two DoFs, and  $\beta$  now corresponds to lateral motion with respect to the direction of aircraft motion. In addition, as with  $\beta$  when  $\mu$  is small, for  $\mu$  near  $90^\circ$  the  $\delta$  DoF is geometrically uncoupled from the other two DoFs. This explains the degree of similarity of Figures 11(a) and (h) for  $\mu = 0$  and  $\mu = 90^\circ$ , respectively, with the roles of  $\delta$  and  $\beta$  exchanged. For intermediate  $\mu$  values, however, the bifurcation diagram is considerably more complex due to the coupling of all three DoFs.

The transition between  $\mu = 0$  and  $\mu = 90^\circ$  in Figure 11 is marked by several qualitative changes of the Hopf bifurcation curves. Moreover, the color map shows how this is associated with changes to the frequency of the bifurcating oscillations. Figure 11(a) shows the two Hopf bifurcation curves for  $\mu = 0$ ; compare with Figure 10. The red curve is clearly associated with oscillations in  $\delta$ , while the other gives rise to stable torsional shimmy oscillations in  $\psi$  along the (blue) section below the other (red) Hopf bifurcation curve. The first qualitative change occurs for a side-stay angle of  $\mu \approx 7^\circ$ , when a loop appears in one of the Hopf curves; see Figure 11(b). Notice further the associated (green) section of this Hopf bifurcation curve, giving rise to oscillations with a frequency near the linear frequency of the out-of-plane DoF  $\beta$ . This Hopf bifurcation curve consequently intersects itself at a double Hopf point (at  $V \approx 145$  m/s), which has a profound influence on the structure of the two-parameter bifurcation diagram, as we will see in the next section. This loop grows to considerable size when  $\mu$  is increased to  $\mu = 20^\circ$ . Moreover, there emerges a nearly horizontal (green) section of this Hopf bifurcation curve associated with oscillations in  $\beta$ ; see Figure 11(c). In effect, the upper boundary of the stability region of the straight-rolling solution is now formed by

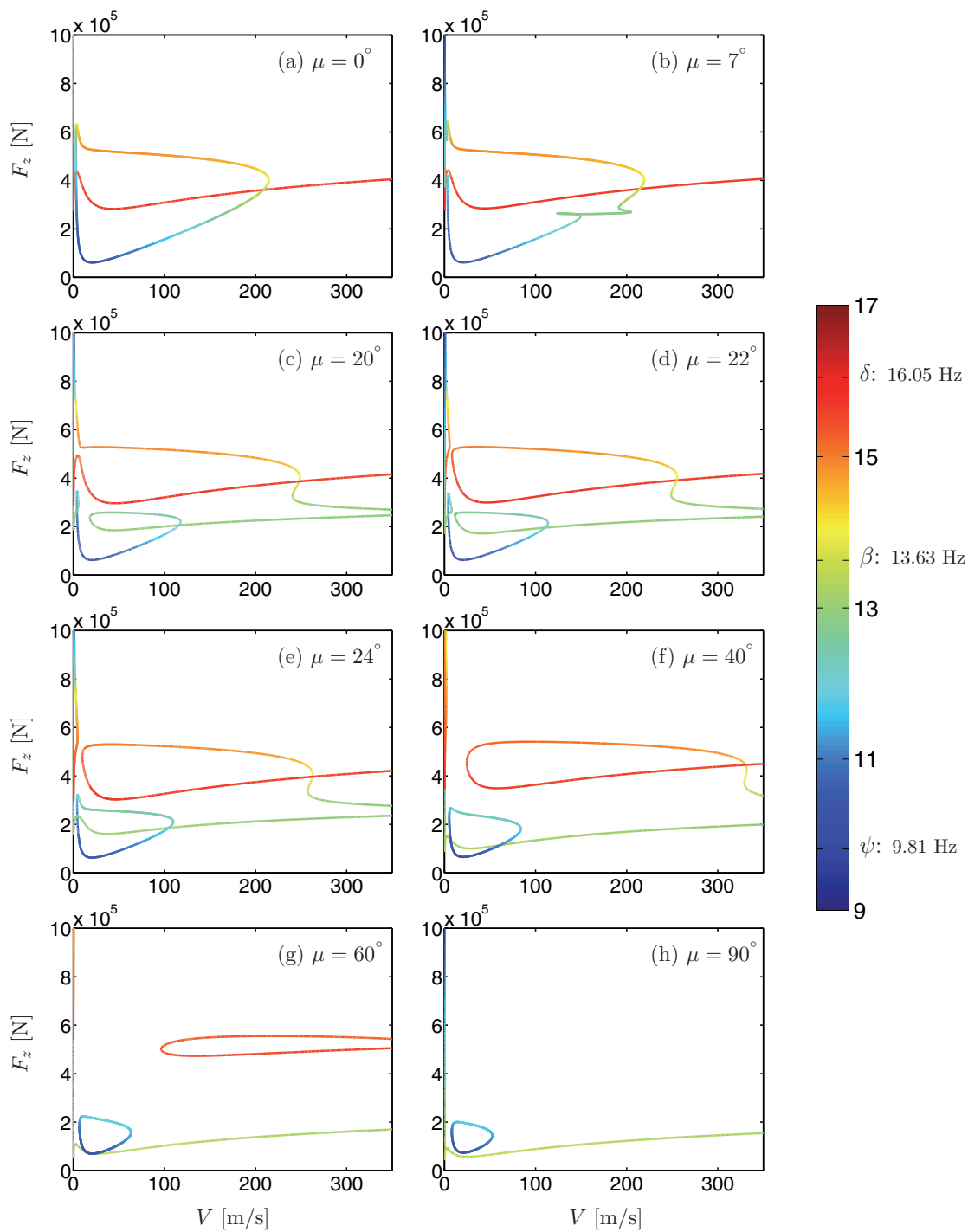


**Figure 11.** The Hopf bifurcation curves in the  $(V, F_z)$ -plane of the MLG for multiple side-stay orientation angles in the range  $\mu \in [0^\circ, 90^\circ]$ ; color represents the frequency of the bifurcating periodic solution as given by the color map.



one and the same self-intersecting Hopf bifurcation curve in the region of interest. Between  $\mu = 20^\circ$  and  $\mu = 22^\circ$  there is a change in the connectivity of the two Hopf bifurcation curves at  $(V, F_z) \approx (7, 5.1 \times 10^5)$ , and another such change occurs between  $\mu = 22^\circ$  and  $\mu = 24^\circ$  at  $(V, F_z) \approx (9, 2.6 \times 10^5)$ ; compare panels (c)–(e) of Figure 11. These changes are due to the fact that the slice  $\mu = \text{const}$  moves through a saddle point of the surface of Hopf bifurcations in  $(V, F_z, \mu)$ -space, and we refer to this phenomenon as a saddle transition of the Hopf bifurcation curves; for other examples of this phenomenon see [54] regarding NLG and [16, 19, 24] more generally. As a result of these transitions we find that for  $\mu = 24^\circ$  and above, a closed (blue) curve of Hopf bifurcations is intersected by a (green) Hopf bifurcation curve—a structure that is remarkably like what we found for  $\mu = 0$  but with the roles of  $\delta$  and  $\beta$  exchanged. Additionally, there is a (red) section of the Hopf bifurcation curve associated with oscillations in  $\delta$ , but at considerably higher values of  $F_z$ ; see Figure 11(e). This (red) section moves toward higher values of  $V$  with increasing  $\mu$ . At the same time the (green) curve of Hopf bifurcations that generates oscillations in  $\beta$  moves toward lower values of  $F_z$ ; see Figures 11(f) and (g). Finally, for  $\mu = 90^\circ$  the section of Hopf bifurcations associated with oscillations in  $\delta$  has left the region of interest in the  $(V, F_z)$ -plane shown in the figure. Moreover, the two remaining curves of Hopf bifurcations no longer intersect each other; see Figure 11(h). As a result, the stability boundary of straight rolling is formed by the (green) Hopf bifurcation curve alone, meaning that as the vertical load is increased one would expect to first see  $\beta$ -shimmy oscillations. Since  $\mu = 90^\circ$ , these oscillations correspond to lateral shimmy.

**4.2. Two-parameter bifurcation diagrams.** Overall, the changes in the Hopf frequency diagram in Figure 11 indicate the sensitivity of the system to variations in side-stay orientation angle  $\mu$ , as well as the increasingly prominent role of the out-of-plane DoF  $\beta$  as  $\mu$  is increased. We now present in Figure 12 the associated two-parameter bifurcation diagrams for each of the eight chosen values of  $\mu$  over the transition from  $\mu = 0$  to  $\mu = 90^\circ$ . Each bifurcation diagram in Figure 12 shows curves of Hopf bifurcations, saddle-node bifurcations of periodic orbits, and torus bifurcations. The shaded regions are the stability regions of torsional  $\psi$ -shimmy (left-slanted), of in-plane  $\delta$ -shimmy (right-slanted), and of out-of-plane  $\beta$ -shimmy (dotted). Comparison of the respective panels of Figures 12 and 11 shows that the Hopf bifurcation curves alone only hint at the stability regions of the different types of shimmy oscillations. The aim of Figure 12 is to illustrate the overall complexity of regions of stable oscillations in the transition from  $\mu = 0$  to  $\mu = 90^\circ$ ; on the other hand, it does not show the details of all transitions of the different bifurcation curves. The overall structure of the bifurcation diagrams in Figure 12 is organized throughout by the codimension-two double Hopf and degenerate Hopf points as well as the associated curves of saddle-node and torus bifurcations of periodic orbits.

Panel (a) of Figure 12 for  $\mu = 0$  is the starting point; it is repeated from Figure 10. Increasing  $\mu$  to  $7^\circ$ , we already find a (dotted) region of  $\beta$ -shimmy oscillations (where the out-of-plane DoF  $\beta$  dominates) in the vicinity of the newly created double Hopf point at  $V \approx 145\text{m/s}$ ; the region is bounded below by the nearly horizontal section of the lower Hopf bifurcation curve, and to the sides by torus and saddle-node bifurcation curves that are associated with double Hopf and degenerate Hopf points; see Figure 12(b). Note that for

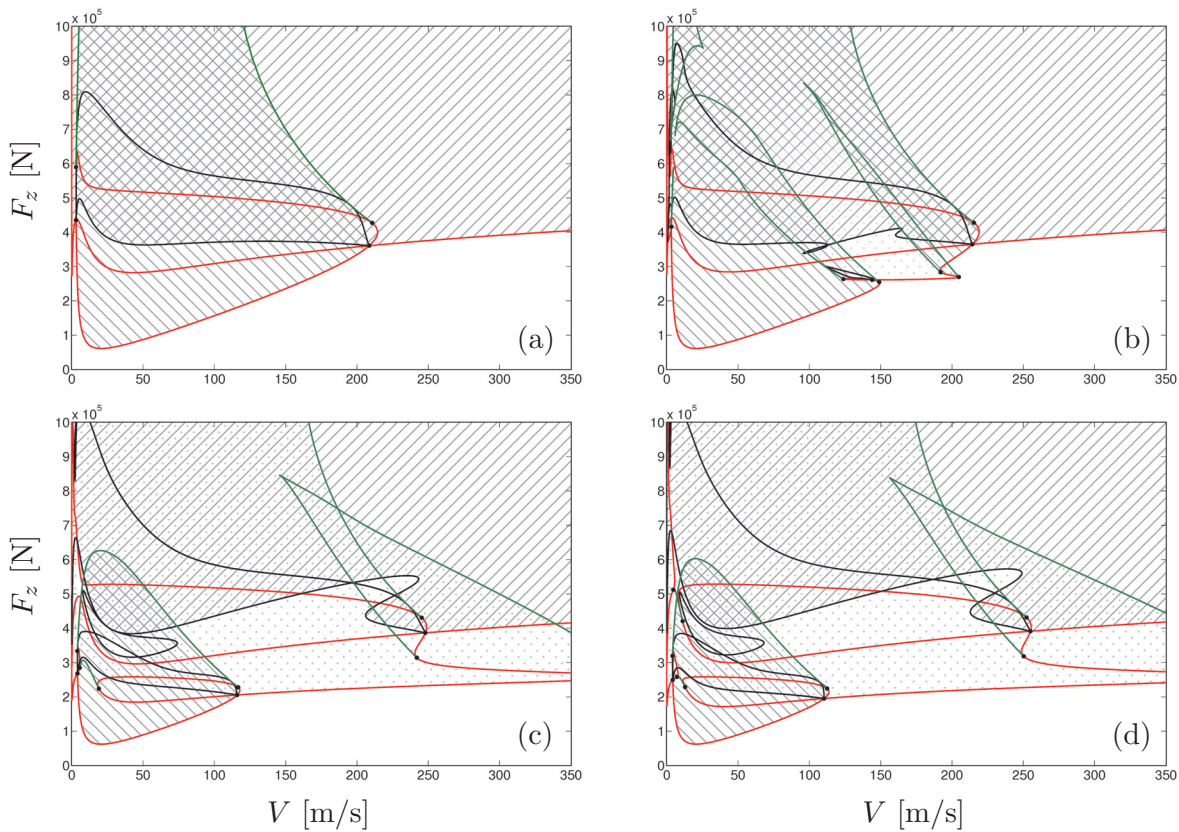


**Figure 12.** Bifurcation diagram of the MLG in the  $(V, F_z)$ -plane for  $\mu = 0$  (a), for  $\mu = 7^\circ$  (b), for  $\mu = 20^\circ$  (c), and for  $\mu = 22^\circ$  (d). Shown are curves of Hopf bifurcations (red), of saddle-node bifurcations (green), and of torus bifurcations (black). In the white region the straight-rolling solution is stable; left-slanted shading denotes stable torsional  $\psi$ -shimmy oscillations, right-slanted shading denotes stable in-plane  $\delta$ -shimmy oscillations, and dotted shading denotes stable out-of-plane  $\beta$ -shimmy oscillations. Panel (a) is repeated from Figure 10.

$\mu = 7^\circ$  there is no clear upper boundary of the region of  $\beta$ -shimmy. Rather, we see a gradual transition in frequency and mode shape from  $\beta$ -shimmy to torsional  $\psi$ -shimmy as the loading force  $F_z$  is increased. Since  $\mu$  is still very small,  $\beta$ -shimmy is effectively longitudinal shimmy. In other words, even a small geometric coupling between the three DoFs may result in the observation of considerable longitudinal oscillations of the MLG.

When  $\mu$  is increased to  $\mu = 20^\circ$ , the region of  $\beta$ -shimmy (which is still largely in the longitudinal direction) increases, both toward larger values of  $V$  and toward larger values of  $F_z$ ; see Figure 12(c). In fact, when  $F_z$  is increased for a velocity  $V$  above 120 m/s, out-of-plane  $\beta$ -shimmy, rather than in-plane  $\delta$ -shimmy, is typically observed. We also note a change in the local connectivity of the torus bifurcation curves due to a saddle transition, that is, a transition through a saddle point in the surface of torus bifurcations in  $(V, F_z, \mu)$ -space; see [54] for another example of such a transition. The bifurcation diagrams for  $\mu = 22^\circ$  and  $\mu = 24^\circ$  are very similar, differing only in the connectivity of the Hopf bifurcation curves; see Figures 12(d) and (e). Here we see the presence of several regions of multiple stability; in particular, for

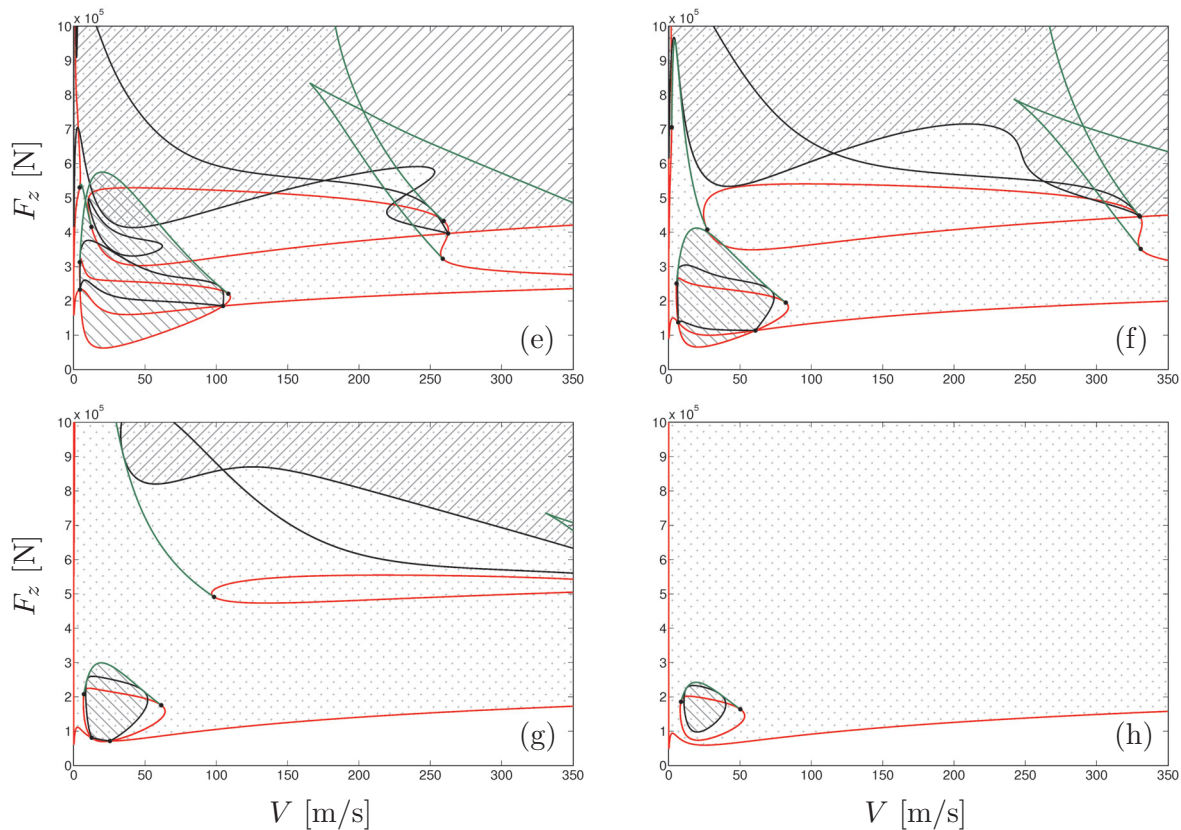


**Figure 12.** *Continued.* Bifurcation diagram of the MLG in the  $(V, F_z)$ -plane for  $\mu = 24^\circ$  (e), for  $\mu = 40^\circ$  (f), for  $\mu = 60^\circ$  (g), and for  $\mu = 90^\circ$  (h).

$\mu = 24^\circ$  we find a region of tristability in which solutions of  $\psi$ -shimmy,  $\delta$ -shimmy, and  $\beta$ -shimmy coexist in the dynamics. A further point of interest in the bifurcation diagrams in Figure 12 is the formation of a local structure of bifurcation curves in the parameter range  $V \in (0, 150)$ ,  $F_z \in (0, 4.5 \times 10^5)$  that is very similar to that found for  $\mu = 0$ . The structure is characterized by the interaction of two Hopf bifurcation curves (one of which is an isola) at two double Hopf bifurcation points with associated torus and saddle-node curves that bound regions of different types of shimmy oscillations; compare panels (e) and (a) of Figure 12. The difference is that for  $\mu = 0$  this structure involves the  $\psi$  and  $\delta$  DoFs, while for  $\mu = 24^\circ$  it involves the  $\psi$  and  $\beta$  DoFs. This is a clear indication of the exchange of the roles of  $\delta$  and  $\beta$  for the dynamics of the MLG. The conclusion is that, even for such relatively small side-stay angles  $\mu$ , the out-of-plane DoF plays a prominent role alongside the in-plane DoF in shaping the dynamics of the MLG system.

When  $\mu$  is increased further to  $\mu = 40^\circ$  and then  $\mu = 60^\circ$ , the isola of Hopf bifurcations associated with torsional oscillations shrinks, and the intersecting Hopf bifurcation curve leading to  $\beta$ -oscillations moves down toward smaller values of  $F_z$ ; see Figures 12(f) and (g). At the same time, the remaining bifurcation curves move further up in  $F_z$ . Finally, the two

lower Hopf bifurcation curves do not intersect any longer (following the transition through a codimension-three degenerate double Hopf bifurcation point), and all other bifurcation curves leave the region of interest of the  $(V, F_z)$ -plane. The result is the bifurcation diagram shown in Figure 12(h) for  $\mu = 90^\circ$ . Apart from a small region of torsional  $\psi$ -shimmy, one finds only stable  $\beta$ -shimmy once the straight-rolling solution becomes unstable. It is an important observation that for  $\mu = 90^\circ$  the MLG has a geometry much like an NLG; indeed, the observation that the (lateral) out-of-plane DoF  $\beta$  is dominant in this case, with no evidence of longitudinal dynamics, agrees well with the results in [52, 53] for an NLG.

We remark that the fixed region in the  $(V, F_z)$ -plane shown in Figures 11 and 12 was deliberately chosen to be quite large, so that the qualitative changes of the bifurcation diagram show (e.g., a more realistic range of the velocity would be  $V \in [0, 80]$  m/s). Notice, however, that qualitative changes of the bifurcation diagram outside the MLG operating region do lead to changes of the observed shimmy phenomena over realistic parameter ranges; for example, we first see out-of-plane motion appearing for  $\mu = 7^\circ$  with the creation the new double Hopf point at  $V \approx 145$ m/s. Therefore, it proves necessary in practice to consider an extended parameter range when exploring the full dynamics of the MLG system. As a final point we note that, as  $\mu$  increases, the nonshaded region representing stable straight-rolling motion of the MLG shrinks. Overall this implies that, for this particular choice of parameters, the system is more likely to experience shimmy as  $\mu$  approaches  $90^\circ$ .

**4.3. Tristable behavior.** We observe in Figure 12 large regions of multiple stability for intermediate values of  $\mu$ . We remark that such behavior is particularly undesirable from a design viewpoint, as sufficient perturbations to the system even near such a region may result in the observation of one of several types of shimmy. This makes it considerably more difficult to design a damper to safeguard against shimmy oscillations as one cannot be sure of the frequency range to expect when the desired straight-rolling solution of the MLG becomes unstable.

To illustrate this point we now focus our attention on the most extreme case: the tristable region near  $(V, F_z) \approx (30, 5 \times 10^5)$  for  $\mu = 24^\circ$  in Figure 12(e). We begin by considering the horizontal slice for  $F_z = 5 \times 10^5$  through the region of interest. Figure 13 shows the one-parameter bifurcation diagram corresponding to this choice of loading force; shown are the bifurcating periodic solutions in terms of the amplitude of the torsional DoF  $\psi$ . We observe the existence of three clearly distinguished periodic solutions in Figure 9. They are labeled according to the type of shimmy oscillation they represent; torsional shimmy oscillations naturally have the highest magnitude of  $\psi$ . There are several regions of bistability, and, importantly, all three types of shimmy oscillation coexist and are stable in the velocity range  $V \in (14.6, 44.2)$ ; this range is bounded on the left by a torus bifurcation of in-plane  $\delta$ -shimmy and on the right by a saddle-node bifurcation of the periodic orbit representing torsional  $\psi$ -shimmy. Notice that the  $\psi$ -shimmy oscillations occur along a closed loop, which is bounded by two saddle-node bifurcations and not connected to the straight-rolling solution. This closed loop may, hence, be missed in a one-parameter continuation that starts from the straight-rolling solution; however, it is easily picked up from knowledge of the two-parameter bifurcation diagram in Figure 12(e).

In the region of tristability the MLG may experience all three types of shimmy oscillations.



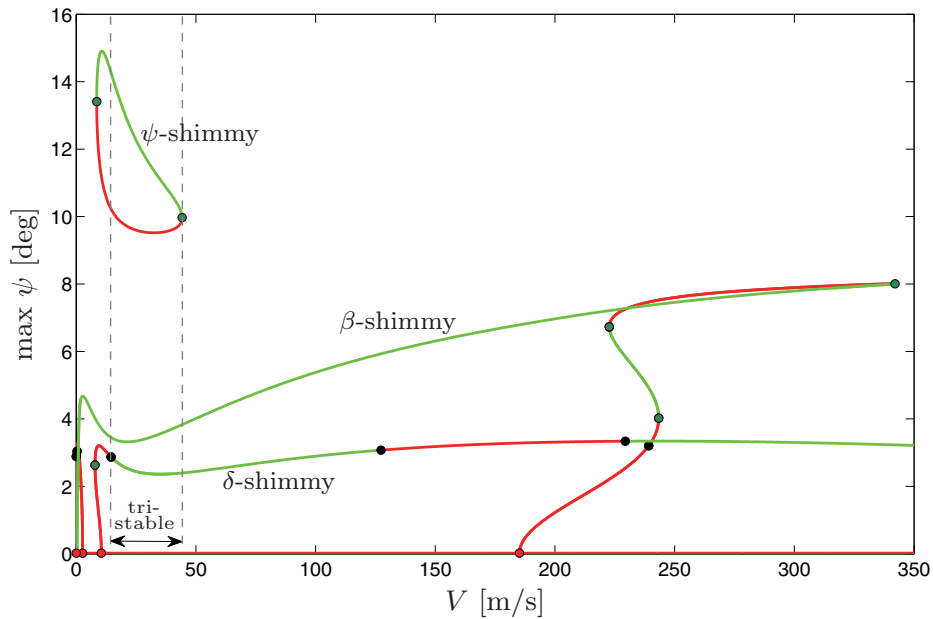


**Figure 13.** One-parameter bifurcation diagram in  $V$  of the MLG with  $\mu = 24^\circ$  and for a vertical force of  $F_z = 5 \times 10^5 \text{ N}$ , showing the maximum of the torsional angle  $\psi$ . The different branches of periodic solutions are labeled according to the type of shimmy oscillations they represent. Stable solutions are green, and unstable solutions are red; also shown are points of Hopf bifurcation (red dots), saddle-node bifurcation (green dots), and torus bifurcation (black dots).

The type that is observed in the dynamics of the landing gear depends on the initial condition as well as on the nature of any possible external perturbations. By performing a numerical integration of the system for a choice of parameters within this region we may verify the coexistence of these three types of shimmy oscillations in the dynamics of the MLG and the possibility of switching between them by suitable perturbations. Figure 14 shows the results of a 60-second simulation run for  $V = 30 \text{ m/s}$  and  $F_z = 5 \times 10^5 \text{ N}$ . As in Figures 7 and 8, the response of the system is shown as time series of  $\psi$ ,  $\tilde{\delta}$ ,  $\tilde{\beta}$ , and  $\lambda$ . The key feature of this simulation run is that we apply two perturbations as follows. At  $t = 20 \text{ s}$  an impulse of 10 kNms is applied to the in-plane DoF  $\delta$ , and at  $t = 40 \text{ s}$  an impulse of 4 kNms is applied to the out-of-plane DoF  $\beta$ . In each case the perturbing force is applied over 0.05 s. These two perturbations are sufficient to drive the system from one periodic solution to another, thus changing the type of shimmy oscillation experienced by the MLG. In particular, we see that the system moves from  $\psi$ -shimmy to  $\delta$ -shimmy following the first perturbation, and then from  $\delta$ -shimmy to  $\beta$ -shimmy as a consequence of the second perturbation. To emphasize the change in behavior we also determine the dominant frequency of the oscillation over the five-second time window prior to each perturbation.

Figure 14 clearly shows that it is possible to switch between the different types of shimmy oscillations by an external perturbation of the MLG. We remark that such perturbations are not unrealistic from a physical viewpoint and may arise from a multitude of sources, including

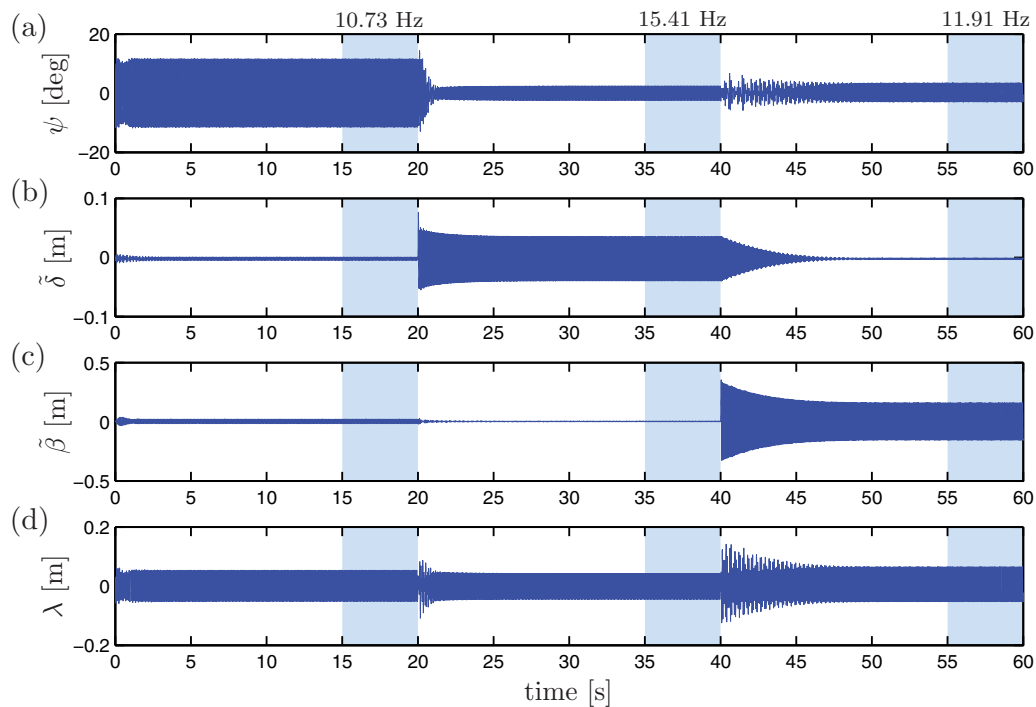


**Figure 14.** Simulation run within the tristable region for parameter values  $(V, F_z) = (30, 5 \times 10^5)$  with  $\mu = 24^\circ$ . Perturbations are applied to the system at  $t = 20$ s to the in-plane DoF  $\delta$  and  $t = 40$ s to the out-of-plane DoF  $\beta$ ; as a result, the system moves between periodic solutions. The dominant frequency of the oscillation in the (shaded) five-second time windows is provided.

heavy braking of the aircraft, contact of the landing gear with a physical object, and traversal over an uneven runway surface. MLG systems may also experience large initial perturbations under heavy or nonsymmetric landing conditions. These kinds of perturbations are largely unpredictable, and, therefore, within regions of multiple stability a degree of uncertainty is introduced into the observable behavior of the MLG.

**5. Discussions and future work.** We have presented a mathematical model of a dual-wheel main landing gear (MLG) system and studied it by means of bifurcation analysis. Specifically, we constructed the bifurcation diagram in the  $(V, F_z)$ -plane of aircraft velocity and loading force on the gear, both of which are key operational parameters. This two-parameter bifurcation diagram provides a wealth of information on the observable dynamics of the MLG, telling us not only in which regions the MLG will oscillate but also which type of shimmy these oscillations represent. From a practical point of view, during take-off or landing the loading force  $F_z$  is a function of the velocity  $V$ : a take-off run corresponds to a path in the  $(V, F_z)$ -plane that starts from a given value of  $F_z$  (determined by the loading of the aircraft) at  $V = 0$  and ends at  $F_z = 0$  at the take-off speed; similarly, a landing corresponds to a path that starts at  $F_z = 0$  at the landing speed and ends at the taxi-speed with a given value of  $F_z$  (again determined by the loading of the aircraft). The bifurcation diagram in the



$(V, F_z)$ -plane can hence be used to evaluate the shimmy behavior of the aircraft for take-off runs and landings under different conditions (loading of the aircraft and/or thrust settings) by considering how the respective curve (which can be measured in practice) intersects the bifurcation diagram.

Moreover, we showed that the influence of other parameters of interest can be studied by considering how the bifurcation diagram in the  $(V, F_z)$ -plane changes. In particular, we explored the effect of changing the orientation of the side-stay as given by the angle  $\mu$ . From a practical point of view, this constitutes a design study as the parameter  $\mu$  is determined at the early stages of the MLG design and cannot be changed during operations. We observed considerable sensitivity of the bifurcation diagram on  $\mu$  when it was changed from  $\mu = 0$  (side-stay perpendicular to direction of travel) to  $\mu = 90^\circ$  (side-stay in line with direction of travel). Most aircraft feature side-stays with  $\mu$  in the range of  $20^\circ$  to  $40^\circ$ , and we found quite a complex bifurcation diagram in this region of side-stay angles. In particular, three different types of shimmy oscillations can be observed in this range of  $\mu$ , which are characterized by the dominance of the torsional, in-plane, and out-of-plane degrees of freedom (DoFs). Moreover, we found considerable regions of multistability, including the coexistence of all three types of shimmy over a large range of realistic velocities. This is of interest from the design point of view, because the different shimmy oscillations are associated with different frequency ranges, a fact which needs to be taken into account, for example, in the design of shimmy dampers.

The study presented here was for a typical landing gear, with parameters adapted from the literature, and its goal was to demonstrate what type of results can be obtained. Clearly, there are many directions for further research. First, some of the parameters that remained fixed here may also differ considerably from MLG to MLG. For example, the horizontal inclination  $\rho$  of the side-stay attachment relative to the attachment point of the main strut also influences the geometric coupling between the DoFs; what is its effect on the dynamics of the MLG? A second direction would be to consider MLG parameters that are more representative of a specific aircraft with a view of optimizing operations. For this purpose a study of the dynamics of the MLG in dependence on additional operational parameters, such as runway conditions or tire pressure, would be suitable. Finally, we mention that there are a number of physical effects that are currently not included in the MLG model presented here, such as the dynamics of the shock absorber and freeplay in bearings. Given the versatility of the modeling approach employed here, it would be relatively straightforward to incorporate such effects into the MLG formulation while still ensuring that it remains amenable to bifurcation analysis.

**Acknowledgments.** The authors thank Phanikrishna Thota for helpful discussions and Etienne Coetzee for sharing his insights, especially concerning the selection of suitable values for the parameters of the model.

## REFERENCES

- [1] J. BAUMANN, *A Nonlinear Model for Landing Gear Shimmy with Applications to the McDonnell Douglas F/A-18A*, Tech. rep. AGARD-R-800, NATO, Neuilly-Sur-Seine, France, 1996.
- [2] J. BAUMANN, C. BARKER, AND L. KOVAL, *A nonlinear model for landing gear shimmy*, in Proceedings of the ASME Winter Annual Meeting, Atlanta, GA, 1991, ASME 91-WA-DSC-14.

- [3] V. BESPALOV, V. METRIKIN, AND M. PEISEL, *On the dynamic stiffness of a landing gear nose strut hydraulic damper system*, *Izvestiya VUZ. Aviatsionnaya Tekhnika*, 32 (1989), pp. 3–6.
- [4] I. BESSELINK, *Shimmy of Aircraft Main Landing Gears*, Ph.D. thesis, Delft University of Technology, Delft, The Netherlands, 2000.
- [5] F. BOHM AND H. WILLUMEIT, *Dynamic Behaviour of Motorbikes*, Tech. rep. AGARD-R-800, NATO, Neuilly-Sur-Seine, France, 1996.
- [6] G. BROULHIET, *The suspension of the automobile steering mechanism: Shimmy and tramp*, *Bull. Soc. Ing. Civ. Fr.*, 78 (1925), pp. 540–554 (in French).
- [7] J. CARROLL AND R. MEHRA, *Bifurcation analysis of nonlinear aircraft dynamics*, *J. Guidance*, 5 (1982), pp. 529–536.
- [8] B. CATINO, S. SANTINI, AND M. DI BERNARDO, *MCS adaptive control of vehicle dynamics: An application of bifurcation techniques to control system design*, in *Proceedings of the 42nd IEEE Conference on Decision and Control*, Vol. 3, IEEE, Washington, DC, 2003, pp. 2252–2257.
- [9] D.-W. CHEN, H.-B. GU, AND H. LIU, *Active control for landing gear shimmy with bifurcation theories*, *J. Vibration Shock*, 29 (2010), pp. 38–42 (in Chinese).
- [10] E. COETZEE, B. KRAUSKOPF, AND M. LOWENBERG, *Application of bifurcation methods for the prediction of low-speed aircraft ground performance*, *J. Aircraft*, 47 (2010), pp. 1248–1255.
- [11] E. COETZEE, B. KRAUSKOPF, AND M. LOWENBERG, *Analysis of medium-speed runway exit manoeuvres*, *J. Aircraft*, 48 (2011), pp. 1553–1564.
- [12] F. DELLA ROSSA, G. MASTINU, AND C. PICCARDI, *Bifurcation analysis of an automobile model negotiating a curve*, *Vehicle Syst. Dynam.*, 50 (2012), pp. 1539–1562.
- [13] M. DENGLER, M. GOLAND, AND G. HERRMAN, *A Bibliographic Survey of Automobile and Aircraft Wheel Shimmy*, Technical report WADC 52-141, Midwest Research Institute, Kansas City, MO, 1951.
- [14] J. DENNIS, *An analytical investigation of damping of landing gear shimmy*, in *Proceedings of the SAE Aerospace Technology Conference and Exposition*, Long Beach, CA, 1990, 902015.
- [15] E. DOEDEL (with major contributions from A. Champneys, T. Fairgrieve, Yu. Kuznetsov, B. Oldeman, R. Paffenroth, B. Sandstede, X. Wang, and C. Zhang), *AUTO-07P: Continuation and bifurcation software for ordinary differential equations*, available at <http://cmvl.cs.concordia.ca/>, 2008.
- [16] H. ERZGRÄBER, B. KRAUSKOPF, AND D. LENSTRA, *Bifurcation analysis of a semiconductor laser with filtered optical feedback*, *SIAM J. Appl. Dyn. Syst.*, 6 (2007), pp. 1–28.
- [17] J. GLASER AND G. HRYCKO, *Landing Gear Shimmy—de Havilland’s Experience*, Tech. rep. AGARD-R-800, NATO, Neuilly-Sur-Seine, France, 1996.
- [18] M. GOMAN, G. ZAGAINOV, AND A. KHRAMTSOVSKY, *Application of bifurcation methods to nonlinear flight dynamics problems*, *Progr. Aerospace Sci.*, 33 (1997), pp. 539–586.
- [19] K. GREEN AND B. KRAUSKOPF, *Bifurcation analysis of a semiconductor laser subject to non-instantaneous phase-conjugate*, *Optics Commun.*, 231 (2004), pp. 383–393.
- [20] D. GROSSMAN, *F-15 Nose Landing Gear Shimmy, Taxi Test and Correlative Analyses*, SAE paper 801239, SAE, Warrendale, PA, 1980.
- [21] A. KANTREWITZ, *Stability of Castering Wheels for Aircraft Landing Gear*, NACA rep. 686, NACA, Washington, DC, 1940.
- [22] M. KLUITERS, *An Investigation into F-28 Main Gear Vibrations*, Fokker report X. 28-430, 1969.
- [23] K. KOENIG, *Unsteady Tire Dynamics and the Application Thereof to Shimmy and Landing Load Computations*, Tech. rep. AGARD-R-800, NATO, Neuilly-Sur-Seine, France, 1996.
- [24] B. KRAUSKOPF AND J. WALKER, *Bifurcation study of a semiconductor laser with saturable absorber and delayed optical feedback*, in *Nonlinear Laser Dynamics: From Quantum Dots to Cryptography*, Wiley-VCH, Berlin, 2012, pp. 161–181.
- [25] H. KWATNY, J.-E. DONGMO, B.-C. CHANG, G. BAJPAI, M. YASAR, AND C. BELCASTRO, *Nonlinear analysis of aircraft loss-of-control*, *J. Guidance Control Dynam.*, 36 (2013), pp. 149–162.
- [26] G. LI, *Modelling and analysis of a dual-wheel nose gear: Shimmy instability and impact motions*, in *Proceedings of the SAE Aerospace Atlantic Conference and Exposition*, Dayton, OH, 1993, 931402.
- [27] D. LIMEBEER, R. SHARP, AND S. EVANGELOU, *The stability of motorcycles under acceleration and braking*, in *Proceedings of the Institute of Mechanical Engineers 215, Part C*, 2001, pp. 1095–1109.
- [28] E. MAIER AND M. RENZ, *Tests on Shimmy with the Nose Landing Gear of the Me 309 and the FKFS Trailer*, N-579 AAF, Air Material Command, Wright Field Technical Intelligence, Dayton, OH, 1947.

- [29] W. MORELAND, *Landing Gear Vibration*, A. F. Technical report 6590, Wright Air Development Center, Dayton, OH, 1951.
- [30] W. MORELAND, *The story of shimmy*, J. Aeronautical Sci., 21 (1954).
- [31] H. PACEJKA, *Analysis of the shimmy phenomenon*, Proceedings of the Institution of Mechanical Engineers: Automobile Division, 180 (1965), pp. 251–268.
- [32] A. PARANJAPPE, N. SINHA, AND N. ANANTHAKRISHNAN, *Use of bifurcation and continuation methods for aircraft trim and stability analysis—a state-of-the-art*, J. Aerospace Sci. Tech., 60 (2008), pp. 85–100.
- [33] N. PLAKHTIENKO AND B. SHIFRIN, *Critical shimmy speed of nonswiveling landing-gear wheels subject to lateral loading*, Internat. Appl. Mech., 42 (2006), pp. 1077–1084.
- [34] J. PRITCHARD, *An Overview of Landing Gear Dynamics*, Technical report NASA/TM-1999-209143, NASA, 1999.
- [35] J. RANKIN, M. DESROCHES, B. KRAUSKOPF, AND M. LOWENBERG, *Canard cycles in aircraft ground dynamics*, Nonlinear Dynam., 66 (2011), pp. 681–688.
- [36] J. RANKIN, B. KRAUSKOPF, M. LOWENBERG, AND E. COETZEE, *Nonlinear analysis of lateral loading during taxiway turns*, J. Guidance Control Dynam., 33 (2010), pp. 1708–1717.
- [37] D. REZGUI AND M. LOWENBERG, *Towards industrialisation of bifurcation analysis in rotorcraft aeroelastic problems*, in AIAA Atmospheric Flight Mechanics Conference, AIAA 2012-4732, 2012.
- [38] L. ROGERS, *Theoretical tire equations for shimmy and other dynamic studies*, J. Aircraft, 9 (1972), pp. 585–589.
- [39] J. ROTTA, *Mathematical Analysis of Wheel Shimmy*, FW-ROT-21-9-44, CADO 66 5241-4, 1944 (in German).
- [40] D. SENSAUD DE LAVAUD, *The fundamental critical speeds of automobiles*, C. R. Acad. Sci. Paris, 184 (1927), pp. 1636–1638 (in French).
- [41] D. SENSAUD DE LAVAUD, *Shimmy, pseudo-shimmy and tramp of an automobile*, C. R. Acad. Sci. Paris, 185 (1927), pp. 254–257 (in French).
- [42] D. SENSAUD DE LAVAUD, *Independently sprung front wheels a remedy for shimmy*, J. Soc. Auto. Engrs., 22 (1928), pp. 623–635.
- [43] S. SHAW AND B. BALACHANDRAN, *A review of nonlinear dynamics of mechanical systems in year 2008*, J. System Design Dynam., 2 (2008), pp. 611–640.
- [44] R. SMILEY, *Correlation, Evaluation, and Extension of Linearized Theories for Tire Motion and Wheel Shimmy*, NACA tech. rep. 1299, NACA, Washington, DC, 1957.
- [45] G. SOMIESKI, *Shimmy analysis of a simple aircraft nose landing gear model using different mathematical methods*, Aerospace Sci. Tech., 8 (1997), pp. 545–555.
- [46] G. STÉPÁN, *Delay, nonlinear oscillations and shimmying wheels*, in New Applications of Nonlinear and Chaotic Dynamics in Mechanics, Solid Mech. Appl. 63, Springer, New York, 1999, pp. 373–386.
- [47] D. TAKÁCS, *Dynamics of Towed Wheels: Nonlinear Theory and Experiments*, Ph.D. thesis, Budapest University of Technology and Economics, Budapest, Hungary, 2010.
- [48] D. TAKÁCS AND G. STÉPÁN, *Experiments on quasiperiodic wheel shimmy*, J. Comput. Nonlinear Dynam., 4 (2009), 031007.
- [49] D. TAKÁCS, G. STÉPÁN, AND J. HOGAN, *Isolated large amplitude periodic motions of towed rigid wheels*, Nonlinear Dynam., 52 (2008), pp. 27–34.
- [50] G. TEMPLE, *Large Angle Shimmy*, ATI 40738, Roy. Aircr. Establ., Farnborough, UK, 1941.
- [51] J. THOMPSON AND F. MACMILLEN, EDs., *Nonlinear flight dynamics of high performance aircraft*, Phil. Trans. Roy. Soc. London Ser. A, 356 (1998), pp. 2163–2333.
- [52] P. THOTA, B. KRAUSKOPF, AND M. LOWENBERG, *Interaction of torsion and lateral bending in aircraft nose landing gear shimmy*, Nonlinear Dynam., 57 (2009), pp. 455–467.
- [53] P. THOTA, B. KRAUSKOPF, AND M. LOWENBERG, *Bifurcation analysis of nose landing gear shimmy with lateral and longitudinal bending*, J. Aircraft, 47 (2010), pp. 87–95.
- [54] P. THOTA, B. KRAUSKOPF, AND M. LOWENBERG, *Multi-parameter bifurcation study of shimmy oscillations in a dual-wheel aircraft nose landing gear*, Nonlinear Dynam., 70 (2012), pp. 1675–1688.
- [55] R. VAN DER VALK AND H. PACEJKA, *An analysis of a civil aircraft main gear shimmy failure*, Vehicle Syst. Dynam., 22 (1993), pp. 97–121.

- [56] B. VON SCHLIPPE AND R. DIETRICH, *Shimmying of a Pneumatic Wheel*, Tech. rep. NACA TM 1365, NACA, Washington, DC, 1941.
- [57] P. WOERNER AND O. NOEL, *Influence of Nonlinearity on the Shimmy Behaviour of Landing Gear*, Tech. rep. AGARD-R-800, NATO, Neuilly-Sur-Seine, France, 1995.
- [58] D. YADOV AND R. RAMAMOORTHY, *Nonlinear landing gear behaviour at touchdown*, J. Dynam. Syst. Measurement Control, 113 (1991), pp. 677–683.